On the design of advanced metal oxide nanomaterials

Lionel Vayssieres

Texas Materials Institute, The University of Texas at Austin,
Austin, TX 78712, USA
Chemical Sciences Division, Lawrence Berkeley National Laboratory,
Berkeley, CA 94720, USA
E-mail: LVayssieres@LBL.gov

Abstract: A novel growth concept and a low-temperature aqueous chemical growth (ACG) thin film processing technique are presented that aim to contribute to the rational fabrication of smart and functional metal oxide particulate thin films and coatings. Such purpose-built materials are modelled, designed, and engineered to match the physical, chemical, and structural requirements of their applications. The concept involves a thermodynamic model monitoring the nucleation, growth, and ageing processes via the chemical and electrostatic control of the interfacial free energy of the system. It enables the control of the size of nano-, meso-, and micro-crystallites, their surface morphology, their orientations onto substrates as well as their crystal structure. The templateless and surfactant-free aqueous synthesis method allows to generate, at large-scale, low-cost, and mild temperatures, advanced metal oxides thin films with designed complexity. It features two- and three-dimensional (patterned) arrays and nanocomposites of transition metal oxides consisting of various isotropic and anisotropic building-blocks with advanced architectures. Such materials are designed to develop a new generation of metal oxide-based composites for optical, optoelectronic, magnetic, and sensor devices.

Keywords: 3-D array; nanostructures; nanocomposite; thin films; nanorod; nanowire; interfacial tension; thermodynamic stability; aqueous solution.

Reference to this paper should be made as follows: Vayssieres, L. (2004) 'On the design of advanced metal oxide nanomaterials', *International Journal of Nanotechnology*, Vol. 1, Nos. 1/2, pp.1–41.

Biographical notes: Lionel Vayssieres received a B.Sc. in Physical Chemistry in 1989 and a Ph.D. in Inorganic Chemistry on thermodynamic growth control of metal oxide nanoparticles in aqueous solutions from the Pierre & Marie Curie University in Paris in 1995. Thereafter, he joined Uppsala University, Sweden as a postdoctoral researcher for the Swedish Materials Consortium on Clusters and Ultrafine particles at the department of physical chemistry and at the department of physics to extend his concepts and develop purpose-built metal oxide nanomaterials as well as to characterize their electronic structure by X-ray spectroscopies at synchrotron radiation facilities. He was invited as a visiting researcher at the department of Chemical Engineering at the University of Texas at Austin on nanocomposite metallic oxides for biosensors, at the department of Biochemistry at Stellenbosch University, South Africa on bio-nanocomposite materials, at the Glenn T. Seaborg center at Lawrence Berkeley National Laboratory on actinide nanomaterials, and at the Texas Materials Institute on metal oxide-based nanomaterials for optical, magnetic, and energy storage and conversion devices. He has (co-) authored over 50 publications and technical reports, presented 40 invited lectures at universities and research institutes and 20 talks at major international conferences worldwide. He is an active referee for the Journal of The American Chemical Society, Chemistry of Materials, Journal of Physical Chemistry B, Angewandte Chemie, Advanced (Functional) Materials, Journal of Nanoscience & Nanotechnology, and the

Journal of Materials Chemistry. He is presently a visiting scientist at Berkeley National Laboratory, USA and at the department of Materials Chemistry at Uppsala University, Sweden, as well as the editor of the International Journal of Nanotechnology (IJNT).

1 Introduction

Nanoscience has reached within the last decade the status of a leading science [1,2] with fundamental and applied research prospects [3] in all basic cognitive sciences such as physical, life, and earth sciences: from chemistry and physics [4,5], biology and medicine [6–9], to astronomy and geology [10,11]. An important feature of nanotechnology is its ability to bridge the crucial dimensional gap between the atomic and molecular scale of fundamental sciences and the microstructural scale of engineering and manufacturing [12]. Accordingly, a vast amount of true multidisciplinary fundamental knowledge is to be explored and linked. It will lead to a fantastic amount of new understanding as well as the fabrication of novel high technological devices in many fields of applications from electronics to medicine. Therefore, the level of man-made technological advance should improve tremendously, that is at a much greater rate than human history has ever experienced. As a result, the societal, educational, and technological implications [13] of nanoscience and nanotechnology are of immense importance, which are attested by the tremendous interests, the major economic efforts, and the national initiatives of many countries around the world.

At the end of the 20th century, most efforts were dedicated to develop synthesis [14,15] and characterization techniques [16–18] to produce and probe nanoparticles of smaller and smaller sizes. Such studies were rewarded by the generation of a new class of materials called quantum dots that are characterized by a zero dimensionality (0-D). Such materials have revealed fascinating size-induced physical and chemical properties due to quantum confinement effects and very high surface-to-volume ratios. One-dimensional (1-D) nanostructures, a new class of low dimensional and anisotropic nanomaterials have emerged recently [19,20]. Their lateral dimension is in the nanometer ranges and their longitudinal dimension ranges from hundreds of nanometer to hundreds of micron. Such characteristics give aspect ratios (length over diameter) of up to several thousand.

The basic goals have been to develop synthesis techniques to produce large quantity of 0-D and 1-D building-blocks in a controllable and fashionable way. Although, the control of the size has empirically and qualitatively been achieved, the strict control of the particle size over orders of magnitude has not yet been clearly demonstrated or quantitatively established. The control of the shape of nanocrystallites also represents an essential task to fulfil. Hitherto, the low-temperature production of anisotropic nanoparticles has mostly been achieved using efficient chemical growth inhibitors, i.e. surfactant [21], or in confined volume, i.e. microemulsion [22] to the detriment of the surface purity. The control of the orientation of anisotropic particles and the capability to generate aligned and ordered nano and microcrystallites onto a substrate are other important challenges. They are currently reached by using masking/patterning techniques such as template [23], lithography [24] or by epitaxial electrodeposition [25] on single crystalline substrates but no low-temperature direct growth method of well-oriented and patterned structures onto various types of substrates have yet been reported. The ability to produce new devices with higher level of design and complexity, combining for instance hollow and ordered nano and microstructures with controlled and tunable porosity is yet

another important challenge to address to develop new devices, such as dye-sensitized photovoltaic cells, dimensionally stable anodes, metal-ion batteries, electrochemical supercapacitors, hydrogen storage devices as well as chemical, gas, and bio-sensors. Several class of materials, including insulators, semiconductors, metallic, and magnetic oxides have been synthesized with tubular micro/nano hollow texture [26–30] using laser-patterning [31], replication and template techniques [32–34], and chemical vapor deposition growth in confined environment [35]. However, such techniques showed strong limitations when up-scaling become a requirement. Indeed, the most serious challenge scientists and engineers have to face to unfold the full potential of applications and prospects of nanotechnology, is the development of sustainable large-scale manufacturing techniques for the time and cost-effective productions of clean and reliable nanomaterials. Although the material development over the last decade has been outstanding due to a plethora of novel and ingenious synthetic techniques for the fabrication of smart and functionalized materials, no large-scale techniques are currently available to meet the economic, environmental, and technological requirements of mass production of nanostructured devices.

In an attempt to take part in the fascinating nanoworld, and to contribute to its ambitious challenges, the present review will expose the outcome of a novel general thermodynamic concept of nucleation, growth, and ageing control and an aqueous thin film processing method (i.e. aqueous chemical growth), which are dedicated to the rational low-cost fabrication of advanced metal oxide particulate thin films and multi-dimensional arrays. The focus of this review is on metal oxides, which represents the most common, most diverse, and probably the richest class of materials in terms of physical, chemical, and structural properties. They include optical, optoelectronic, magnetic, electrical, thermal, electrochemical, photoelectrochemical, mechanical, and catalytic properties. Such diversity originates from the more complex crystal and electronic structures of metal oxides compared to other class of materials. The main reasons are found in the variety of oxidation states, coordination numbers, symmetry, crystal-field stabilization, density, stoichiometry, and acid-base surface properties, metal oxides exhibit. They truly are fascinating compounds, capable of insulating, semiconducting, metallic, and magnetic behaviours with continuous or sudden transitions between these states. The combinations of such variety of properties and applications with the unique effects of nanomaterials of low-dimensionality make the studies of novel metal oxide nanostructures a very important issue of research and development from both fundamental and industrial standpoints. For instance, developing the ability and competence to hierarchically order, connect, and integrate metal oxide 0-D quantum dots and 1-D nanowires and nanotubes, in functional networks, thin film coatings, as well as 2- and 3-D arrays is of major importance to generate and manufacture practical nanodevices. Such future devices will certainly revolutionize materials science and engineering due to their unique design, architecture, and physical properties as well as their capability to connect the nanoworld to the microworld.

2 Background

2.1 Theoretical concepts

The goal is to develop a strategy to reach the rational design of nanomaterials with modelled and controlled particles size, morphology, orientation, and crystal structure,

i.e. purpose-built nanomaterials [36], to probe, tune, and optimise their physical and chemical properties. In our view, to achieve such ambitious challenge, the most pertinent parameter to monitor is the interfacial free energy of the system.

2.1.1 Size control

The main idea is to tune the thermodynamics and kinetics of nucleation, growth, and ageing of a system by controlling experimentally its interfacial tension [37]. For instance, the ability to segregate the nucleation and the growth stage enables to control the monodispersity of nanoparticles. Indeed, performing an aqueous precipitation far from the typical point of zero charge (PZC) of the investigated metal oxide allows an enhanced control of the nucleation, growth, and ageing processes.

According to the acid-base properties of metal oxide surfaces, increasing (or decreasing) the pH of precipitation/dispersion from the PZC will increase the surface charge density by adsorption of hydroxyl ions (or protons). Consequently, the chemical composition of the interface will change, and so the interfacial tension of the system. In addition, a high ionic strength will contribute to a further increase of the surface charge density. This is understood by considering the electrostatic forces at the interface; indeed by increasing the ionic strength of the medium, a more effective screening effect of the interfacial charged sites will allow further surface sites to develop a charge. In such case, the surface charge may therefore reach its maximum charge density, which ultimately depends on the oxygen structure and composition of the interface. At maximum charge density, the interfacial tension of the system will reach a minimum. Thermodynamic colloidal stability may thus be reached resulting in a considerable lowering of the secondary ageing processes, henceforth preventing the nanoparticle size (and distribution size) to increase as well as avoiding crystal phase (and morphological) transformations.

Any adsorption phenomenon at interface decreases the surface (or interfacial) tension γ. Such effect is described quantitatively by the Gibbs adsorption equation:

$$\mathrm{d}\gamma = -\sum_i \Gamma_i \, \mathrm{d}\mu_i$$

where Γ represents the superficial adsorption density and μ the chemical potential of the adsorbed species *i*. Based on such equation, a model was developed to quantifies the variation of the water-oxide interfacial tension with the chemical composition of the interface and the dispersion conditions:

$$\Delta\gamma = \gamma - \gamma_0 = 25.7\sigma_{\max}\mathrm{Ln}\left[1 - I\left(\frac{0.117\sinh(1.15\Delta\mathrm{pH})}{\sigma_{\max}}\right)^2\right] - 6\sqrt{I}\left[\cosh(1.15\Delta\mathrm{pH}) - 1\right]$$

where γ is expressed in mJ/m^2, the ionic strength, *I*, in mol/l, and the maximum surface charge density $\sigma_{\max}$ in C/m^2. Assuming a zero interfacial tension at equilibrium, by analogy with microemulsion systems where ultralow surface tensions at equilibrium have been reported [38], a quantitative treatment has been developed to obtain the thermodynamic stability conditions of the water-oxide system for precipitations of metal ions in basic medium [37,39]:

$$\mathrm{PZIT} = \mathrm{PZC} + 2.46 + 2\log\sigma_{\max} - \log I$$

For precipitation occurring between the point of zero charge (PZC) and the point of zero interfacial tension (PZIT), the surface charge does not reach its maximum, and consequently the interfacial tension remains positive and the system is submitted to secondary growth and ageing. As a result, the nanoparticles will evolve in solution, that is, their size will increase with time, and their crystal structure may be subjected to phase transformations. This is the *unstable* region of the precipitation. However, at precipitation pH ≥ PZIT, i.e. the *stable* region, the nanoparticles are thermodynamically stabilized, and consequently secondary growth phenomenon such as Ostwald ripening does not occur. No longer submitted to ageing, the nanoparticle size is finite and is directly related to the precipitation conditions such as pH and ionic strength at a given temperature and precursor concentration.

By consideration of the nucleation and growth processes which rule the generation of solid phases from solutions, a maximum is found for the first derivative of the free enthalpy of nucleation with respect to the number of precursors (which essentially represents the particle size). Such a maximum depends on the interfacial tension at the cubic power:

$$\Delta G^{*} = \frac{16}{3}\frac{\pi\,\bar{v}^{2}\,\gamma^{3}}{\left(RT\ \mathrm{Ln}\ S\right)^{2}}$$

Therefore, reducing the interfacial tension leads to an important lowering of the nucleation energy barrier, which in turn leads to the decrease of the nanoparticle size. A large stage of nucleation of very small particle accompanied by a very short stage of growth is predicted. As a result, the average nanoparticle size (and its distribution) is expected to decrease substantially.

The experimental verification of such concepts was performed on the controlled aqueous precipitation of crystalline magnetite (Fe_3O_4) nanoparticles at room temperature [40]. It clearly illustrated that the thermodynamic stability of metal oxide nanoparticles is a reality. It also demonstrated that the average particle size may experimentally be monitored (and semi-empirically predicted) over an order of magnitude from 1.5 nm to 15 nm with narrow size distributions. The excellent agreement between theory and experiments sustained the accuracy and relevance of the general and efficient growth control concepts of metal oxide nanoparticles under low interfacial tension conditions. Moreover, such conclusions entitled great expectations for a future development of advanced particulate nanomaterials devices with tailored and optimised physical/ chemical properties.

In summary, the strict monitoring of the precipitation conditions during the entire synthesis yields to a very simple, yet efficient, control of the nanoparticle size and its distribution in solution.

2.1.2 Shape control

Moreover, when the thermodynamic stabilization is achieved, not only the size is tailored but also the shape as well as the crystallographic structure may be controlled. For instance, at low interfacial tension, the shape of nanoparticles does not necessarily require being spherical; indeed very often nanoparticles develop a spherical morphology to minimize their surface energy because the sphere represents the smallest surface for a

given volume. However, if the synthesis and dispersion conditions are suitable (i.e. yielding to the thermodynamic stabilization of the system), the shape of the crystallites will be driven by the symmetry of the crystal structure as well as by the chemical environment, and various morphologies may therefore be developed. Manipulating and controlling the interfacial tension enables to grow nanoparticles with sizes and shapes tailored for their applications. Applying the appropriate solution chemistry (precursors and precipitation/dispersion conditions) to the investigated transition metal ion along with the natural crystal symmetry and anisotropy or by forcing the material to grow along a certain crystallographic direction by controlling chemically the specific interfacial adsorptions of ions and/or ligand and crystal-filed stabilization, one can reach the ability to develop purpose-built crystal morphology.

2.1.3 Crystal structure control

In addition to particle size and shape control, the precipitation of nanoparticles at low interfacial tension allows the stabilization of oxide and oxyhydroxide metastable crystal structures. Crystal phase transitions in solution generally operate through a dissolution-recrystallisation process to comply with the surface energy minimization requirement of the system. Indeed, when a solid offers several allotropic phases and polymorphs, it is typically the one with the highest solubility and consequently the lowest stability, (i.e. the crystallographic metastable phase), which precipitates first. This is understood by considering the nucleation kinetics of the solids. At a given supersaturation ratio, the germ size is as small (and the nucleation rate as high) as the interfacial tension of the system is low. Thus, given that the solubility is inversely proportional to the interfacial tension, the precipitation of the most soluble phase and consequently the less stable thermodynamically, is therefore kinetically promoted. Due to its solubility and metastability, this particular phase is more sensitive to secondary growth and ageing, which leads to crystallographically more stable phases, essentially by heteronucleation. This is typically the case for aluminum hydroxide (boehmite $\rightarrow$ bayerite or gibbsite), titanium dioxide (anatase $\rightarrow$ rutile), or ferric oxyhydroxides (goethite, akaganeite, or lepidocrocite $\rightarrow$ hematite). Secondary growth and ageing processes are delicate to control and the phase transformations appear within a few hours to a few days in solution, whence the resulting undesired mixing of allotropic phases and polymorphs. However, by careful consideration of the precipitation conditions (i.e. at thermodynamically stable conditions), such phenomena may be avoided when nanosystems are precipitated at low interfacial tension [37].

In summary, by adjusting the experimental conditions to reach the thermodynamic stability of a system, the nanoparticle size, shape, and crystal structure may be tuned and optimised. It allows the functionalised design of nanomaterials and the ability to quantitatively probe the influence of such parameters on the physical and chemical properties of metal oxide nanoparticles and nanoparticulate materials.

2.2 Aqueous chemical growth thin film processing technique (ACG)

By applying the above mentioned concepts to the thin film processing technology, a novel and inexpensive bottom-up approach namely, aqueous chemical growth (ACG) technique has been developed to produce functionalised thin films and coatings of metal

oxide materials onto various substrates at low cost and mild temperatures [41]. Such a method allows generating advanced nano-, meso-, and micro-particulate thin films as well as two- and three-dimensional arrays, without any template, surfactant, or external field and without any specific requirements in substrate activation, thermal stability, or crystallinity. Given that the crystallites are nucleating and growing directly from the substrate at mild temperatures, a large choice of substrates (e.g. amorphous, single crystalline, polycrystalline, transparent, conducting, flexible etc.) is offered. Such diversity provides a higher degree of nanomaterials engineering and design.

The synthesis involves the hydrolysis-condensation of hydrated metal ions [42] and complexes (inorganic polymerisation) and their heteronucleation onto substrates. Experimentally, the aqueous chemical growth simply consists of heating an aqueous solution of metal precursors (salts or complexes) at a given ionic pH and ionic strength, in the presence of substrates at mild temperatures (below 100°C) in a closed bottle as illustrated in Figure 1. Therefore, such method does not require expensive and complicated set-up or hazardous high-pressure containers. It is entirely recyclable, safe, and environmental-friendly, since only water is used as solvent. Such a process avoids the safety hazards of organic solvents and their critical evaporation and potential toxicity. In addition, since no organic solvents or surfactants are present, the purity of the as-prepared thin films is substantially improved. The residual salts are easily washed out by water due to their high solubility. In most cases, no additional heat or chemical treatments are necessary, which represent a significant improvement compared to the sol-gel process as well as surfactant, template and membrane-based synthesis methods. The utilization of temperature and chemical sensitive substrates required by certain applications is therefore allowed.

Figure 1 The aqueous chemical growth (ACG) thin film processing technique: I. Introduction of the bare substrates or thin films; II. Total (or partial) immersion of the substrates in selected aqueous solutions of metal salt precursors at room temperature; III. Heat treatment at constant temperature in a laboratory oven below 100°C; IV. Generation of nano-, meso-, and micro-particulate thin films of large physical area

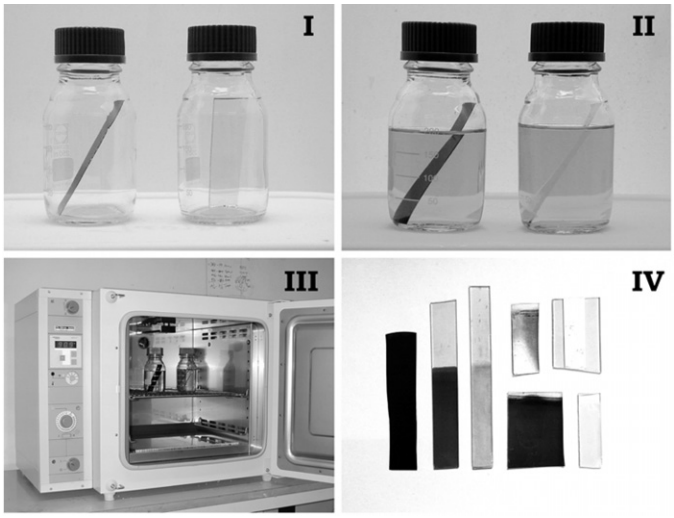

2.2.1 Orientation control

To develop the capability of growing nano- to micro-particulate thin films from aqueous solution and controlling the orientation of large arrays of anisotropic nanoparticles onto a substrate, one has to consider the differences between homogeneous and heterogeneous nucleation phenomena. In most cases, homogenous nucleation of solid phases from solutions requires a higher activation energy barrier and therefore, heteronucleation is promoted and energetically more favourable. Indeed, the interfacial energy between two solids is generally smaller than the interfacial energy between a solid and a solution, and therefore nucleation may take place at a lower saturation ratio onto a substrate than in solution. Nuclei will grow by heteronucleation onto the substrate and various morphologies and orientation monitoring can be obtained by experimental control of the chemical composition of the precipitation medium. To illustrate and demonstrate such capabilities, the example of an anisotropic crystal is taken and the possibilities of experimentally monitoring its orientations onto a substrate using the aqueous chemical growth thin film processing technique are exposed hereafter.

Anisotropic building blocks with multi-angular orientation onto substrates may be generated when the number of nuclei is exceedingly limited by the precipitation conditions (through the chemical and electrostatic monitoring of the interfacial tension). The system will promote twinning and the preferential epitaxial three-dimensional growth of the rods along their easy axis from a very limited number of nuclei will induce a star-shape (or flower-shape) morphology as illustrated in Figure 2a.

Anisotropic building blocks with a perpendicular orientation onto substrates may be obtained when the number of nuclei is slightly limited by the precipitation conditions. The slow appearance of a limited number of nuclei will allow the slow growth (according to the crystal symmetry and relative face velocities) along the easy direction of crystallization. As a result, a condensed phase of anisotropic nanorods parallel to the substrate normal will be generated as illustrated in Figure 2b.

Figure 2 Schematic representation and SEM images of the effect of the number of nuclei on the orientation of anisotropic crystallites grown onto substrates by ACG

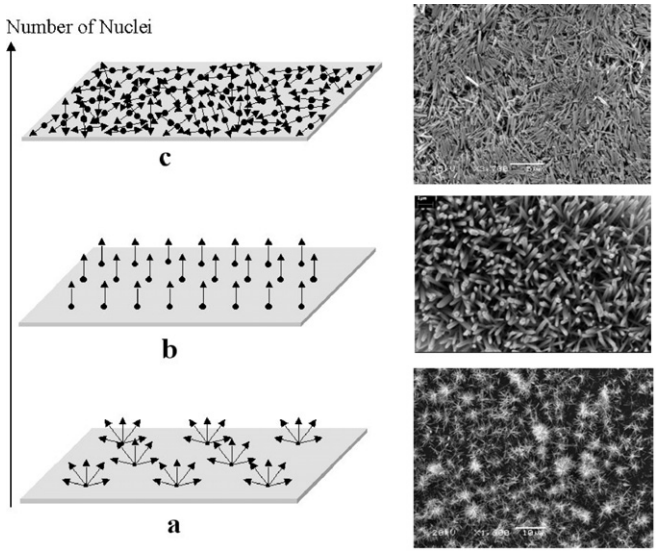

Anisotropic building blocks with a parallel orientation onto substrates can be obtained when the nucleation rate is enhanced by the precipitation conditions. Indeed, the fast appearance of a large number of nuclei will result in a rapid two-dimensional growth. The stacking of anisotropic nanoparticles with random orientation between each other but with an overall perpendicular orientation with respect to the substrate normal is therefore promoted as illustrated in Figure 2c.

The ability to design materials consisting of anisotropic nanoparticles of different orientations enables the experimental studies of the angular dependence influences on the physical/chemical properties and electronic structure of materials and gives further opportunities for materials design and engineering (e.g. increased dimensionality).

2.2.2 Thin film coverage

The coverage of particulate thin films is easily monitored with such synthesis. Indeed, very low coverages (sub-monolayer) are obtained by monitoring the synthesis time as well as the precursor concentration in the early stages of the growth process. Full coverage of the substrate (monolayer and multilayers) is obtained within few hours to few days depending on the temperature, synthesis time, and precursor concentrations (Figure 3). Coverage control is an important feature of a thin film processing technique. Many applications request the adjustment and fine tuning of thin film thickness, materials porosity, and quantity. For instance, catalysts and supports for catalyst require a homogeneous distribution of the material for the sake of efficiency and economic purposes. The fabrication of multibandgap thin films also requires a fine tuning of materials coverage, thicknesses, and porosity. Therefore, the optical properties (e.g. absorption or refractive index) of the entire device may be tuned and optimised by adjusting the coverage of materials n vs. materials $n + 1$. The ability to perform multi-depositions as well as the layer-by-layer growth of thin films is an important ability for nanoengineered materials. Any thin films (at any stage of their synthesis) can be used as a support or a template for the fabrication of multi-component or multilayer thin films

Figure 3 Schematic representation and SEM images of the effect of synthesis time on the surface coverage of thin films grown by ACG

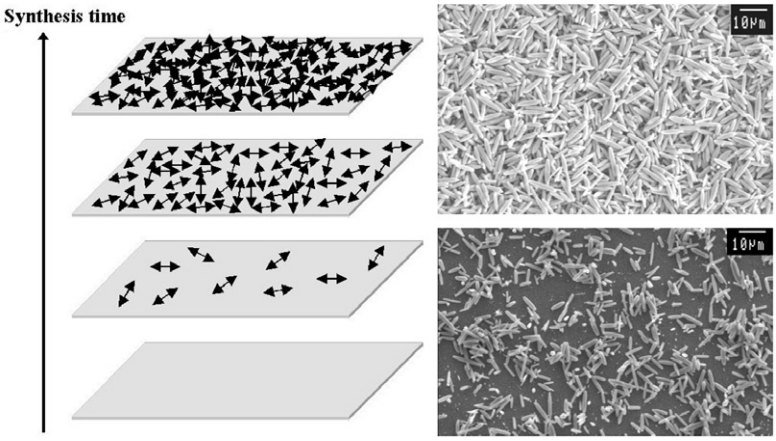

consisting of various morphologies and/or various chemical compositions. Figure 4 illustrates the ability to form composite thin films where two different oxides of various morphologies are present. Figure 5 shows the fabrication of a multilayer thin film where two metal oxide nanomaterials are grown on the top of each other to create a multibandgap thin film.

The complete thin film architecture may thus be modelled, designed, and fabricated to match the requirement of high technological applications. In addition, it allows developing novel thin film integrated devices with improved overall efficiency as well as functional coatings.

Figure 4 Schematic representation and SEM images of the ability of ACG to fabricate composite thin films

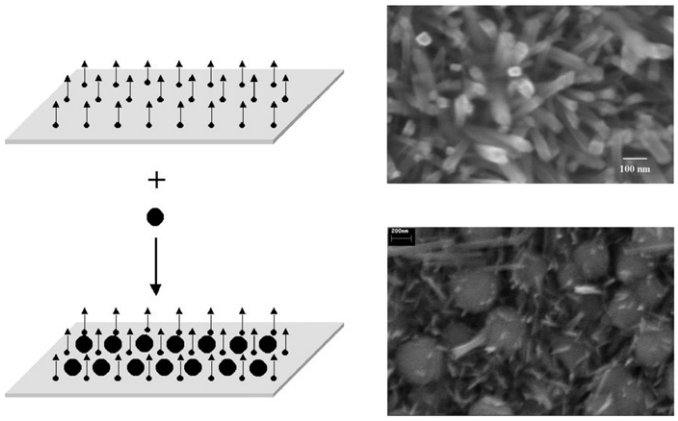

Figure 5 Cross-section SEM images of the ability of ACG to generate multilayer thin films. A thin film consisting of hematite nanorods was grown by ACG onto a nanoporous TiO_2 thin film deposited onto a commercial conducting glass substrate

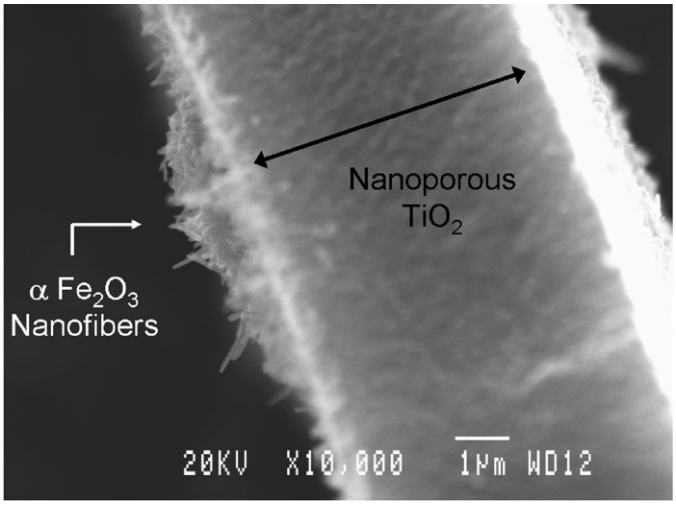

2.2.3 Adhesion

Growing thin films directly onto substrates substantially improves the adhesion properties and mechanical stability of the as-prepared thin films compared to the standard solution and colloidal deposition techniques such as spin and dip coating, chemical bathing, screen printing, or doctor blading. Moreover, given that such materials grow by homogeneous nucleation in solution from molecular scale compounds (i.e. condensed metal complex), they are virtually growing by heteronucleation on any type of substrate. It goes without saying that the overall mechanical stability of the thin films does vary from substrate to substrate, but in most cases, a relatively good adhesion is observed. When a strong adhesion is required and when the substrate allows it, heat treatments may be performed to improve the linkages of the thin films onto their substrates by annealing and sintering processes.

2.2.4 Patterning

The ability to develop non-lithographic techniques to pattern, to assemble, and to integrate nanomaterials as functional 3-D networks is an important challenge scientists have to face to develop functional and practical nanodevices. The fabrication of patterned metal oxide 3-D arrays is possible with the ACG technique by a general consideration of the chemical, physical, and structural affinities and interactions of substrates, metal precursors, and synthesis conditions. Figure 6 shows various examples of the patterning ability on ZnO nanomaterials. Well-defined stars and stripes of ZnO nanorods of various patterns are obtained onto the silicon wafer substrates. Further demonstrations of such ability are currently in progress. Very promising results are foreseen for the low-cost fabrication of large patterned array of transition metal oxides as well as for the creation of novel optoelectronic nanodevices [43].

2.2.5 Bio-compatibility

ACG is also potentially very interesting due to the compatibility of water and aqueous solutions, controlled pH, and mild temperatures to biological compounds and their applications. It is indeed possible to create novel composite bio-nanomaterials consisting of metal oxides and biologically active chemical compounds (see Section 3.9).

2.2.6 Large-scale manufacturing

A crucial feature, if not the most, is the large-scale manufacturability of a synthesis technique. Many parameters have to been taken into account to identify such ability. However, up-scaling the ACG method is definitely realistic. First, the theoretical concepts as well as the experimental technique are applicable to all water-soluble metal ions likely to precipitate in solution. Second, the exclusive use of water as solvent, the mild temperatures required and the low cost of precursors (metal salts) make of such a technique, a suitable candidate for large-scale manufacturing of low cost nanomaterials and devices. As it is, advanced thin films with physical areas as large as several tens of centimetres square are obtained. The utilization of larger containers and larger substrates will provide the ability to generate much larger physical areas.

Figure 6 SEM images of various 3-D patterned arrays of metal oxide (ZnO) grown by ACG onto commercial silicon wafers

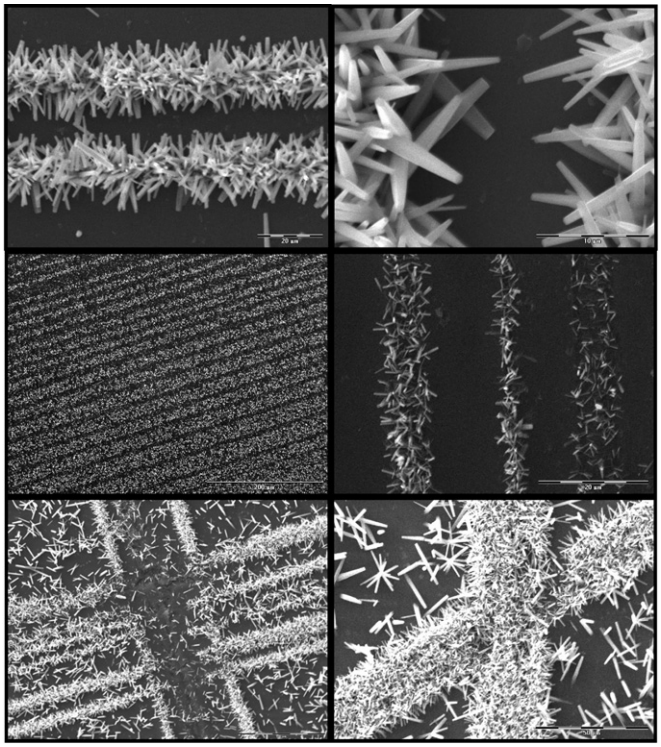

Thermodynamic stability of metal oxide nanoparticles and the aqueous chemical growth thin film processing technique have been successfully applied to the design of metal oxides and metal oxide-based materials and composites of the first-, second-, and third-row of transition metal ions such as Ti, Cr, Mn, Fe, Co, Ni, Cu, Ru, and Ir as well as post-transition metals such as Sn and Zn. More complex (and doped) oxides are currently under investigation.

3 Achievements

3.1 2-D arrays of isotropic chromium sesquioxide mesoparticulates

Trivalent chromium oxides are widely studied for a variety of catalytic applications [44–46], and are commonly used as a green pigment and as coatings to overcome industrial problems of micro-alloying of reactive elements due to their water repellent [47] and refractory properties [48]. More striking is the spontaneous non-reciprocal reflection of light that was theoretically predicted in the late sixties [49], but first observed experimentally on α-Cr_2O_3 in 1993 [50], although numerous attempts were carried out in high-T_c superconductors to detect such time-parity violation effects.

α-Cr_2O_3 occurs in nature as the mineral Eskolaite, which was discovered in the late fifties [51] and named after the Finnish scientist P. Eskola. It crystallizes in the trigonal-hexagonal scalenohedral crystal system, space group $R\text{-}3c$, and is isostructural with α-Al_2O_3 (corundum), α-Fe_2O_3 (hematite), and V_2O_3 (karelianite). The lattice is built

on a hexagonal close packed (HCP) array of oxygen in which four out of every six available octahedral sites are occupied by Cr. The octahedral and tetrahedral sites are located directly above one another in the HCP lattice and the tetrahedral sites are empty. The octahedra share faces along a threefold axis and are distorted to trigonal antiprisms due to the Cr-Cr repulsion across the shared face (inset Figure 7). This atomic arrangement gives the Cr^{3+} ions the centro-symmetric D_{3d} point group symmetry and leads to a highly dense structure offering high polarizability, high refractive index, and intense colour. With their $3d^3$ electronic configuration, the chromium ions experience strong crystal-field stabilization energy. The atomic structure and electronic configuration confer to this sesquioxide a unique combination of electronic, optical, and magnetic properties. Its electronic structure is of particular interest because of the simultaneous characteristics of a charge-transfer insulator (bandgap 4.7–5 eV) and a Mott-Hubbard regime due to the location of Cr ions in the middle of the first-row transition series [52]. α-Cr_2O_3 shows antiferromagnetic ordering below $T_N \sim 307$ K with no net magnetic moment and consequently, magnetoelectric effect [53], that is, electrically polarized by magnetic fields and magnetized by electric fields. Consequently, a better fundamental understanding of its electronic structure and unique non-reciprocal optical properties [54,55] is crucial to validate recent theories of optical effects in antiferromagnetic materials [56,57]. In addition, such knowledge may contribute to develop better magneto-electric and magneto-optic devices and to optimise the efficiency of solar thermal collectors [58] and tunnel junction barriers [59]. To achieve such goals, high quality particulate thin films and two-dimensional arrays consisting of stoichiometric, non-aggregated (antiferro) meso/micro-particles with well-defined surface morphology and narrow size distribution rather than (superpara) nanoparticles are required.

The current synthetic processing techniques to generate thin films of α-Cr_2O_3 include electrodeposition [60], magnetron sputtering [61], UHV thermal oxidation [62], MOCVD [63], and laser irradiation [64]. However, the generation of monolayer arrays consisting of monodispersed and non-interacting spherical particles onto various substrates is not achievable with such techniques.

Figure 7 SEM images and XRD pattern of a 2-D sub-monolayer array of α-Cr_2O_3 grown by ACG onto commercial silicon wafers. The inset shows the corundum crystal structure [65]

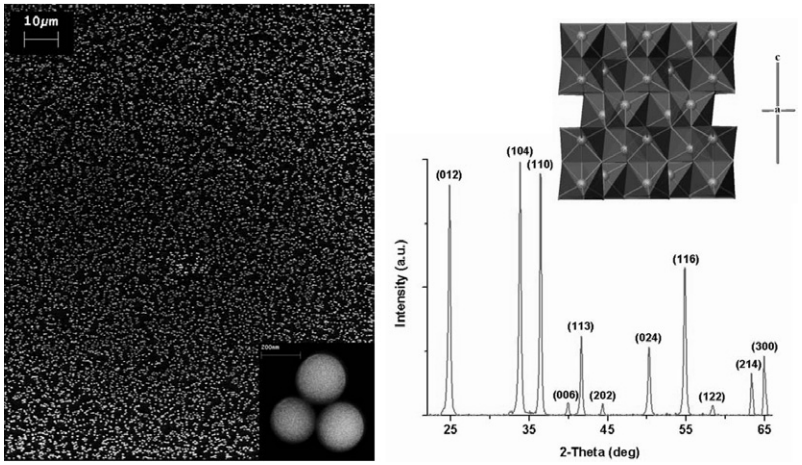

ACG was used to create large 2-D sub-monolayer arrays of isotropic nanoparticles of hydrated chromium(III) oxide as well as its sesquioxide after a short heat treatment in air. The achievement of such arrays requires a very slow growth process from solutions of low supersaturation and low ionic strength. Therefore, the synthesis consisted of the slow deprotonation of the *blue-violet* hexa-aqua chromium(III) ions, $[Cr(H_2O)_6]^{3+}$, the condensation of its neutral complexes, most probably $[Cr(OH)_3(H_2O)_3]^0$ and $[Cr_2(OH)_6(H_2O)_4]^0$, the growth of its *blue-grey* hydrated oxide by heteronucleation onto the substrates at mild temperatures, and finally the annealing in air to its thermodynamically stable *green* sesquioxide corundum phase, α-Cr_2O_3 [65]. Figure 7 shows the SEM images of the arrays grown onto Si wafers. A submonolayer of well-defined, monodispersed and non-aggregated spherical particles of α-Cr_2O_3 of typically 250 nm in diameter is observed onto the substrates. The inset clearly illustrates that no contact is present between crystallites. The particles are randomly and homogeneously distributed in very large arrays, *ca* 20 cm^2. According to electron and X-ray diffractions, eskolaite (corundum, JCPDS 38-1479) was the only crystallographic phase detectable and it showed high crystallinity (Figure 7).

The optical properties of a sub-monolayer of non-interacting, spherical mesoparticles of narrow distribution of α-Cr_2O_3 grown by ACG onto transparent substrate were investigated by UV-visible spectroscopy. The absorption spectrum showed well-defined and well-resolved absorption peaks centred at 375 nm and 495 nm which originate from the $^4A_{2g} \rightarrow {}^4T_{1g}$ and $^4A_{2g} \rightarrow {}^4T_{2g}$ electronic transitions respectively. Such transitions appeared significantly blue shifted compared to the reported values in the literature [66]. Simple nonlinear statistical multi-peak fitting led to broad shoulders centred at, 700 nm, attributed to the $^4A_{2g} \rightarrow {}^2T_{1g}$, $^2E_{2g}$ electronic transitions, and at 950 nm which extented into the near IR region, that are characteristic of Cr^{3+} ions in distorted octahedral environment.

The optical properties of Cr^{3+} ions ($3d^3$) in α-Cr_2O_3 originate from *d-d* electronic transitions between the splitted lower triply degenerated t_{2g} levels and the upper doubly degenerated e_g levels of the fivefold degenerated 3*d* orbitals of the chromium ions in the centrosymmetric D_{3d} point group. The free ion *LS*-terms in D_{3d} symmetry are ^4F, ^2G and ^4P. The ground state is ^4F, which splits into $^4A_2$, $^4T_2$, and $^4T_1$. The excited state is ^2G and splits into ^2E, $^2T_1$, $^2T_2$, $^2A_1$. The optical transitions originate from the *strong* spin-allowed but parity-forbidden $^4A_{2g} \rightarrow {}^4T_{2g}$ and $^4A_{2g} \rightarrow {}^4T_{1g}$ transitions as well as from the *weak* spin and parity-forbidden transitions $^4A_{2g} \rightarrow {}^2E_{2g}$, and $^4A_{2g} \rightarrow {}^2T_{1g}$ [67]. The bandwidths of such transitions are usually large due to the strong electronic coupling to vibrations of the local environment as well as the stoichiometry, size, surface morphology, and monodispersity of the samples. The most striking feature of spin magnetoelectric α-Cr_2O_3 is the spontaneous non-reciprocal optical effects such as gyrotropic birefringence and respective dichroisms where both, time and parity symmetry, are broken. In addition, strong second harmonic generation signal [68] originating from the $^4A_{2g} \rightarrow {}^4T_{2g}$ transition of Cr^{3+} ions in α-Cr_2O_3 due to the two-photon excitation of $^4T_{2g}$ levels below T_N [69] is observed and used to image the antiferromagnetic domains and determining magnetic symmetry.

Due to the synthesis process, the narrow size distribution and well-defined non-interacting crystallites arranged as a 2-D sub-monolayer, the main absorption features appeared well-resolved and blue shifted, offering a great opportunity for the in-depth study of the strong resonant second harmonic generation signal. Such designed materials may also have potential impact as model systems in the fundamental understanding and

modelling of antiferromagnetic ordering by light [70] and in particular, for experimental studies of non-reciprocity in reflection and transmission of light in α-Cr_2O_3 [71], and large third-order optical nonlinearities of transition metal oxides [72]. In addition, such very large arrays could be of great interest for heterogeneous catalysis as well-defined catalysts, and support for catalysts as well as for probing and demonstrating the relationships between magnetic state, surface morphology, crystal structure, and catalytic activity [73].

3.2 3-D arrays of 1-D iron oxide and oxyhydroxide

Iron compounds are essential materials in chemistry, biology, and geology due to their large occurrence in nature [74]; in water [75], plants [76], minerals [77] and clay minerals [78], and sediments [79] and sedimentary rocks [80]. Iron oxides play a central role in geochemistry of soil [81], in planetary science [82], and contribute for instance, to the oxidation of sedimentary organic matter [83]. In their various allotropic forms, iron oxides and oxyhydroxides represent important basic and raw materials [84]. Their large abundance, non-toxicity, low-cost, high refractivity, and various colors, contribute to their popularity as polishing agents, and for colorants (red and yellow ochre) for the pigment and paint industry. Indeed, iron oxides are one of the most commonly used coloured pigments in the paints and coatings market [85]. They are also widely studied in the alloys and steel industries [86] and in metallurgy [87], as catalysts [88–90] and photocatalysts [91] as well as for magnetic storage devices, cathodes for primary and secondary batteries [92], chemical flame suppressant [93] and for the crucial industrial, economical and environmental issue of corrosion [94]. The thermodynamically stable crystallographic phase of ferric oxides is the sesquioxide hematite (α-Fe_2O_3), which represents the most important ore of iron considering its high iron content and its natural abundance. Designing iron(III) oxide materials with novel morphologies is of great fundamental importance for basic physical, earth, and life sciences and of relevance for various fields of industrial and technological applications.

The fabrication of novel and smart iron oxide materials was demonstrated by the production of quantum-size 1-D nanorods arranged in highly oriented 3-D bundles onto many different substrates [95]. Such purpose-built materials were designed to produce low cost photoelectrochemical devices such as photovoltaic cells [96] as well as photocatalytic cells for photo-oxidation of water [97–98]. Hematite is theoretically an ideal candidate for photoelectrochemical applications. Its low cost, abundance, chemical and photocorrosion stability as well as its low band gap (around 2 eV) make a very attractive candidate for such applications. Unfortunately, after many studies over several decades, which included highly porous nanomaterials [99], the photo-efficiency remained at very low values, mostly due to the high level of electron-hole recombinations in the solid and at grain boundaries.

Our strategy involved the design of hematite nanomaterials consisting of anisotropic 1-D nanoparticles (nanorods and nanowires). The purpose of such design intended to lower the recombination processes by eliminating the grain boundaries generated by isotropic nanoparticles. In addition, designing nanorods with a perpendicular orientation onto the substrate would facilitate the transport of photogenerated electrons to the back contact through a direct pathway rather than a random transport across spherical nanoparticles. Finally, tailoring the diameter of the nanorods with the hole (minority carrier) diffusion length would drastically reduce the electron-hole recombinations.

Indeed, the shorter the distance the holes have to reach the interface, the faster the recombination with the redox species in solution. Such process will enable a better generation and collection of photogenerated electrons, and therefore, a higher photo-efficiency will be reached.

The synthesis involved the perpendicular growth and thermodynamic stabilization of the anisotropic and metastable phase of ferric oxyhydroxide (akaganeite, β-FeOOH) according to the theoretical concepts. Subsequently, a phase transition was induced by a heat treatment in air. As a result, hematite designed with the required anisotropic oriented configuration (i.e. 3-D nanorod array) was obtained. Stabilization of the akaganeite phase is required because the growth of β-FeOOH from solutions is subjected to a structural and a morphological change from rod-like nanoparticles to α-Fe_2O_3 spherical or cubic ones [100]. However, lowering the interfacial tension significantly reduced the ageing process and suppressed the phase and morphological transformation into hematite. According to the general concept, by lowering the pH of precipitation to a minimum value (i.e. where the precipitation is barely occurring), that is, far from the PZC and by setting the ionic strength of the synthetic medium at a high concentration of non-complexant ions, stabilized and highly charged anisotropic nanoparticles of akaganeite were obtained with controlled orientations. According to DSC/DTA thermal analysis, a subsequent heat-treatment in air above 390°C provided the thermodynamically stable crystallographic phase of ferric oxide (i.e. hematite) skillfully designed with the required nanorod morphology [95].

Matching the diameter of the nanorods with the hole diffusion length of hematite [101] was obtained by taking advantage of the structural properties of akaganeite. β-FeOOH crystallizes in the tetragonal system (space group *I4/m*, a = 10.44, c = 3.01 Å). The structure can be described as a tunnel structure (similar to α-MnO_2) hosting H_2O or Cl^- and based on a defected close packed oxygen lattice with three different kinds of oxygen layers. Every third layer is only two-third occupied with rows of oxygens missing along the c-axis. The cation occupation of the octahedral sites between the other anion layers is in double rows, but separated by single rows of empty sites along c. The octahedral cation sites remain between the third anion layer and its neighbour layers are completely filled. This structural configuration produces di-octahedral chains, which are arranged about the four-fold symmetry c-axis. The chains share vertices along their edges, forming square-cross section tunnels, some 5 Å on edge. The crystals are elongated along the c-axis and of rod-like morphology. These crystals have empty cores that produce a square channel of about 3 nm on a side. The anisotropic crystals form a bundle called a somatoid. Such structural particularity will be use to generate quantum nanorod of hematite with diameter matching the hole diffusion length. Dehydration of β-FeOOH at high temperature leads to the α-Fe_2O_3 phase (Figure 8), which crystallizes in the trigonal crystal system and is isostructural with α-Cr_2O_3.

The synthesis was performed at 0.15 M of iron, pH 1.5 and 1 M sodium nitrate at 95°C [95]. Aligned single-crystalline nanorods of typically 5 nm in diameter, self-assembled as bundle of about 50 nm in diameter were obtained in fairly perpendicular fashion onto the transparent conducting substrate and arrange in very large uniform arrays (Figure 9). The length of the nanorods, which essentially represented the thickness of a homogeneous monolayer, could be experimentally tailored to any required dimension of up to about 1 μm by varying the time and/or the temperature of ageing (i.e. nanorods of 100 nm in length was produced after about an hour at 95°C). The aspect ratio is 1 to 20 for the nanorod bundle and 1 to 200 for the individual nanorods.

Figure 8 Crystal structure representations of the solid phase transition of the tetragonal tunnel structure of akaganetite (β-FeOOH) to the rhombohedral dense structure of hematite (α-Fe_2O_3)

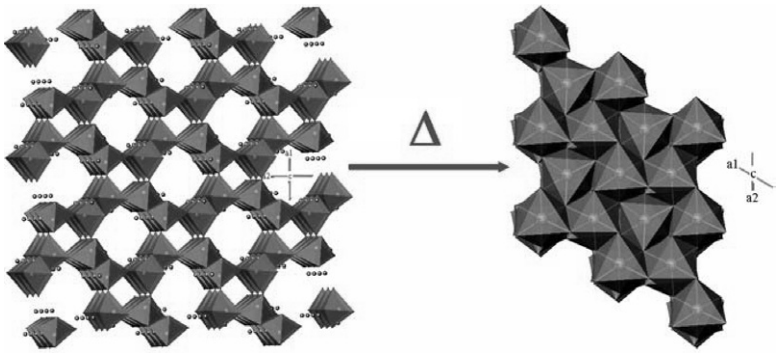

Figure 9 SEM images of perpendicularly oriented nanorod bundles of hematite (500 nm in length) grown by ACG onto a transparent conductive oxide substrate (left). TEM image of the fine structure of a hematite nanorod bundle (50 nm in diameter) consisting of single crystalline nanowires of 5 nm in diameter (right)

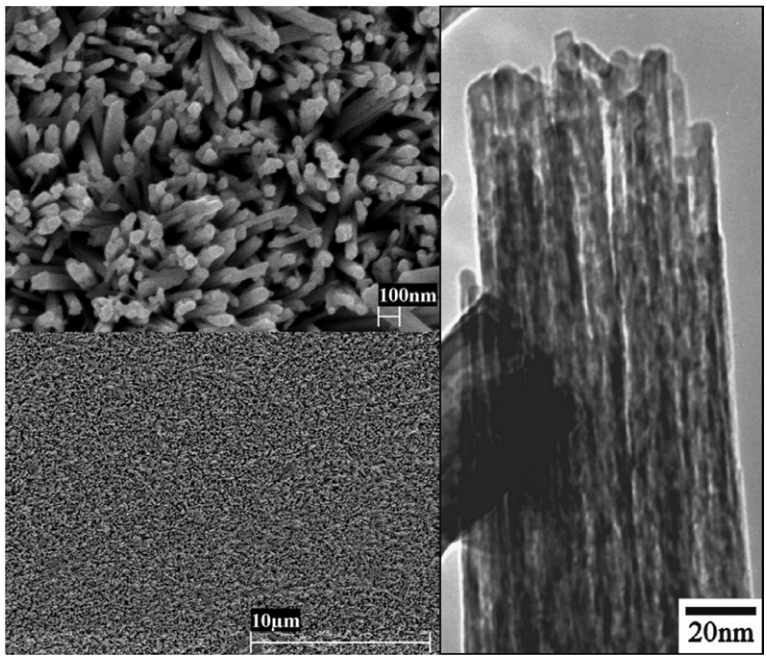

As previously stated, such quantum rods arranged in oriented 3-D bundles of several tens of cm^2 patterned arrays (Figure 10) have been designed for photoelectrochemical applications. Indeed, since the array features an oriented and direct, grain boundary free electron pathway and given that the fine diameter of the nanorods matches the minority carrier diffusion length, the fast electron-hole recombination is prevented, allowing fast generation, transfer and collection of photogenerated electrons. Incident photon-to-electron

conversion efficiency (IPCE) as high as 60% at 350 nm was obtained in a 3-electrode set-up [96], which represents an improvement of more than 100 times compared to previously reported data on nanostructured hematite in similar operating conditions [99]. In addition, sandwich-type cells (2-electrode set-up) were fabricated. An open circuit voltage of 0.3 V and short circuit currents of several hundreds of μA were recorded at an illumination of 100 W/cm^2. Although, the overall efficiency remained low (0.2%) due to the very low thickness and hence the absorption of the thin film, such cells constituted the first demonstration of a wet iron oxide photovoltaic cells.

Figure 10 SEM and still camera images of patterned 3-D arrays consisted of perpendicularly oriented bundles of crystalline nanorods of hematite grown by ACG onto F-SnO_2 glass substrate

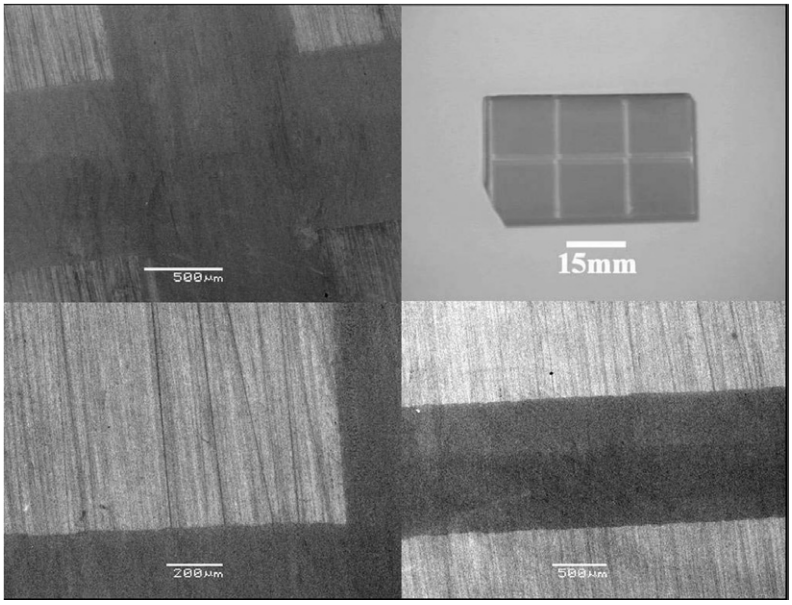

Various thin film textures were achieved by varying the conditions of aqueous chemical growth. Figure 11 summarizes some of the achievements in hematite nanomaterials design.

3.3 3-D arrays of iron spinel oxide-sesquioxide nanocomposite

3-D arrays of iron oxyhydroxide (akaganeite) nanorods were utilized as templates to fabricate a nanocomposite of iron oxides. The hematite arrays were subjected to a simple and controlled mild reduction reaction in solution at room temperature. As a result, novel iron oxide nanocomposites were fabricated. They are composed of the spinel phase (cubic *Fd3m*) of iron oxide (Magnetite, Fe_3O_4) and of its sesquioxide phase (Hematite, α-Fe_2O_3). Figure 12 shows the SEM images of such designed nanocomposite materials. The thin films consist of oriented hematite nanorods with randomly and homogeneously dispersed aggregates of magnetite nanoparticles. Such nanocomposites possess magnetic and optical properties and are currently under investigation to develop novel magnetic-semiconducting sensor devices [102].

Figure 11 SEM images of 3-D arrays of crystalline hematite anisotropic nanoparticulates of various textures grown by ACG onto conducting substrates

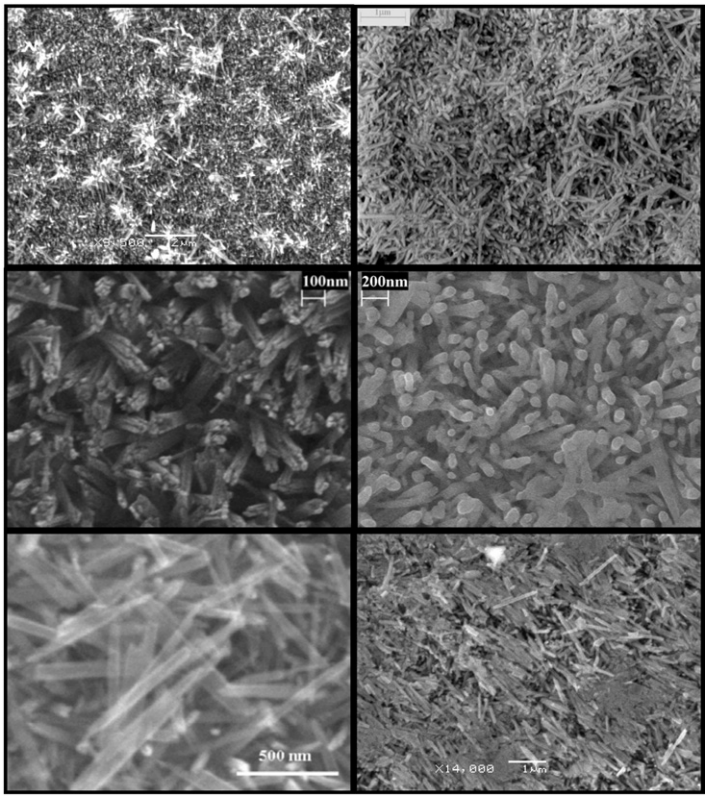

Figure 12 SEM images of nanocomposite thin films of α-Fe_2O_3–Fe_3O_4 consisting of oriented hematite nanorods and magnetite spherical nanoparticles grown onto transparent conducting F-SnO_2 glass

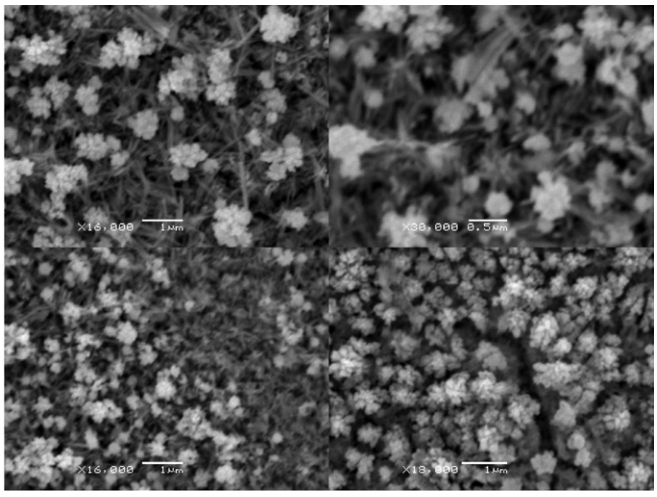

3.4 3-D arrays of anisotropic ferromagnetic α-Fe

In another attempt to generate novel magnetic materials, 3-D arrays of iron oxyhydroxide (akaganeite) nanorods were used to create highly oriented ferromagnetic arrays of elemental iron (α-Fe) [103] onto various substrates. The same synthesis strategy was used, that is, the perpendicular growth and stabilization of akaganeite nanorods, followed by a reduction in H_2 atmosphere at 300°C to obtain the crystalline cubic phase of iron metal with the anisotropic and oriented designed (Figure 13). Such relatively low temperature of reduction originated from the very narrow diameter of the individual akaganeite nanorods and overall porosity of the array which facilitate the diffusion of hydrogen. In addition, a simple crystallographic transformation pathway exits between tetragonal β-FeOOH (001)-elongated nanorods and cubic α-Fe (110)-elongated nanorods which significantly contributed in lowering the activation energy of the reduction process.

Figure 13 SEM and TEM images, schematic representation, diffraction patterns, and magnetic measurements of ferromagnetic 3-D arrays consisting of oriented nanorods of iron (α-Fe) grown onto sapphire substrates [105]

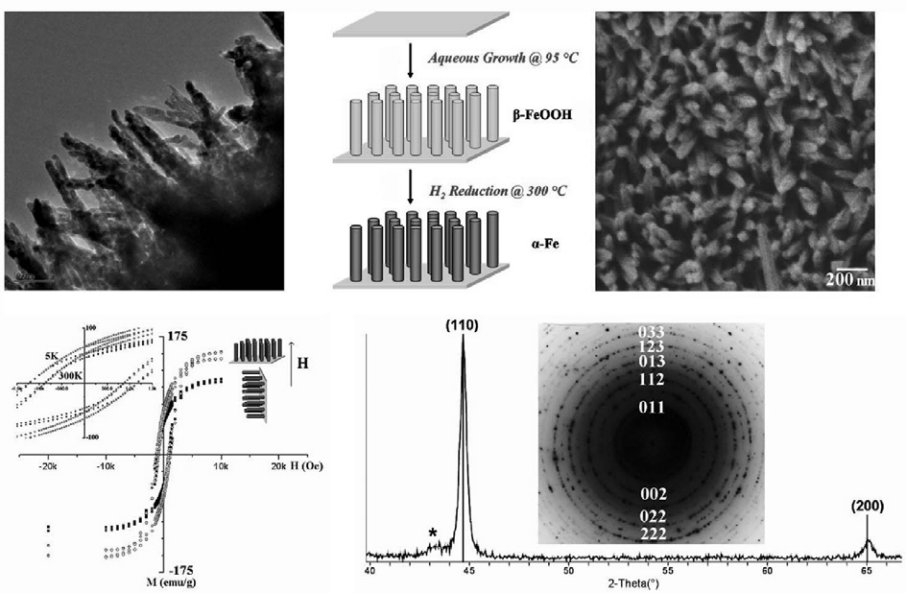

TEM and SEM studies confirmed that the thin films were made of 1-D nanorods oriented normal to the substrate surface (Figure 13). The nanorods seemed to consist of small anisotropic crystalline nanoparticles of about 5–10 nm in diameter and about 15–30 nm in length, stacked as columns, and bundled as nanorods that was 30–40 nm in diameter and of 0.8–1 μm in length. The nanorods were homogeneously distributed onto the entire surface of the substrate regardless of its crystallinity and physical surface area. EDS analysis confirmed that the nanorods consisted of elemental iron. X-ray and electron diffraction patterns corresponded to α-Fe (cubic system, space group *Im3m*) with a lattice constant of 2.86 Å as observed in bulk iron samples (e.g. JCPDS 06-0696). No evidence of strong crystallographic texture among the Fe grains was observed and the high

magnification TEM study suggested that the volume difference between the Fe rods and their precursor remained as voids between the Fe crystallites.

Magnetic measurements were carried out on a superconducting quantum interference device (SQUID) as a function of temperature (FC and ZFC protocol) and as a function of the applied field at 5 and 300 K for fields oriented perpendicular and parallel to the 3-D array of iron nanorods (grown on single crystalline sapphire substrates). The nanorod arrays showed a strong, temperature-independent magnetization, with a slightly higher saturation magnetization value for the parallel orientation compared to that for the perpendicular orientation. This suggested that the easy axis was along the nanorod axis. At field of 10 kOe and above, the samples showed saturation magnetization values of 115 and 150 emu/g, for the samples oriented perpendicular and parallel to the magnetic field, respectively. The samples showed high coercivity values of 1200 Oe at 5 K and 900 Oe at 300 K without significant difference for the two orientations. The remanent magnetization was around 50 emu/g with a relatively good squareness of the hysteresis loop and a high hysteresis loss (inset Figure 13).

Such large nanoengineered crystalline arrays of oriented iron nanorods with high remanence and high coercivity could be of interest for magnetic recording as well as for magneto-electronic sensors considering their simple and cost-effective fabrication. Besides the technological interest of oriented metallic and magnetic nanowires, fundamental understanding of their electronic structure and magnetic properties (e.g. quantum confinement effects, metal-to-insulator transition as well as the effect of shape anisotropy on the magnetization reversal) is crucial for further device optimisations. Such investigations are currently being pursued at synchrotron facilities by polarization-dependent X-ray absorption, resonant inelastic X-ray scattering, and circular dichroism.

3.5 3-D arrays of iron-chromium sesquioxide nanocomposite

Iron-chromium sesquioxide composites are important materials for corrosion science, and have been under exploration to investigate the artificial passivation of stainless steel and binary alloys and their thin film dissolution processes [104–106] as well as for their catalytic properties [107].

In our study, the goal was to create a smart thin film material with extended optical absorptivity, strong resistance to photocorrosion, and fast electron transfer for optical filters, solar absorbers, catalytic, and photoelectrochemical applications. Therefore, Fe-Cr sesquioxide nanocomposites were developed. Indeed, the combination of hematite (α-Fe_2O_3), which transmitted color is red, and eskolaite (α-Cr_2O_3), which is green should give stable dark-brown nanocomposite materials with extended optical absorption properties in the visible range.

The synthesis involved the heteroepitaxial growth of the corundum α-Cr_2O_3 array directly onto the corundum α-Fe_2O_3 nanorod array [108]. The isostructural characteristic between the two sesquioxides contributed to the homogeneity and mechanical stability of the nanocomposites. Figure 14 shows SEM images of the nanocomposite thin films which consist of monodispersed and non-aggregated spherical nanoparticles of eskolaite of 250 nm in diameter, homogeneously distributed in the perpendicularly oriented array of hematite nanorod bundles. As predicted, optical measurements of the nanocomposites showed an extended absorption profile with a substantial improvement compared to bare hematite thin films. Absorption of, 100% of the photons at wavelength below 500 nm,

between 85% and 60% below 650 nm and up to 40% at 800 nm was achieved (Figure 15). High photovoltaic and photocatalytic efficiencies are expected and currently under examination.

Figure 14 SEM images of nanocomposite thin films of α-Fe_2O_3–α-CrO_3 consisting of hematite nanorods and eskolaite spherical nanoparticles grown by ACG on transparent conducting F-SnO_2 glass

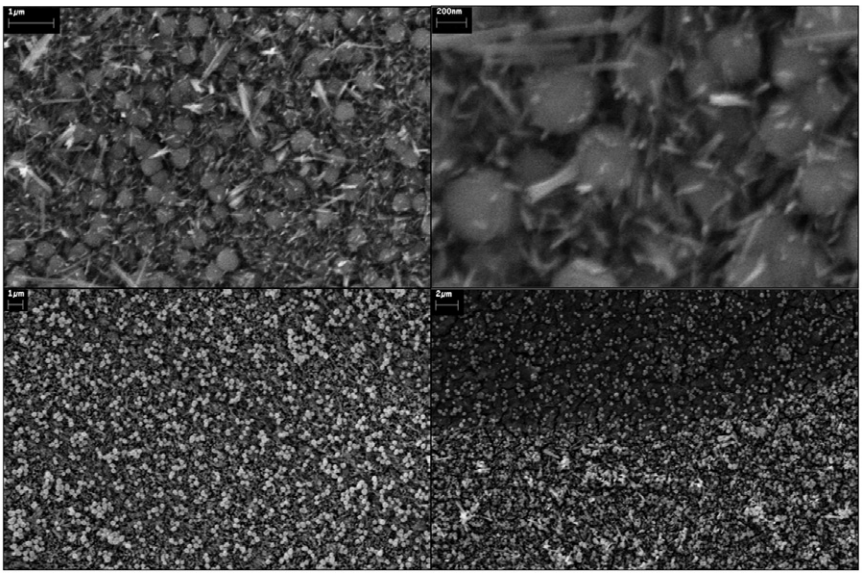

Figure 15 Optical absorption profile of α-Fe_2O_3 and α-Fe_2O_3–α-Cr_2O_3 nanoparticulate thin films grown by ACG onto transparent conducting glass. The contribution of the substrate was subtracted

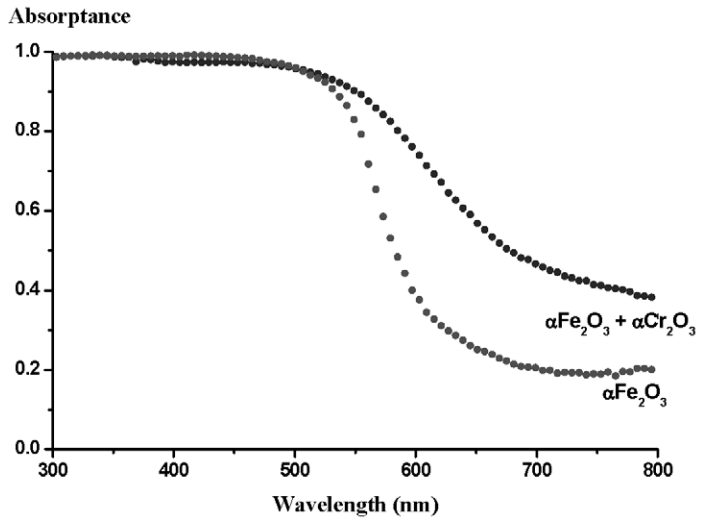

3.6 3-D arrays of manganese oxide and oxyhydroxides

Manganese is the second most abundant metal on earth (after iron). Manganese oxide minerals are of great economic and environmental significance [109]. Indeed, about 30 different Mn oxides, hydroxides, and oxyhydroxides minerals have been identified in nature. Hence, they play an important role in groundwater chemistry as well as in the precipitation, transport, and dissolution of soils and sediments. They are also used as catalysts, pigments (for bricks), and plant fertilizers. However, their greatest technological use is for portable energy storage and conversion devices such as alkaline and lithium-ion batteries [110–114] and they are sought to replace Ni-based compounds in batteries due to their low cost, low-toxicity, and the large occurrence of their polymorphs and allotropic phases. Besides representing the most important raw compounds in battery materials, Mn oxides and oxyhydroxides are playing a crucial role in the battery operation. Indeed, the charge-discharge processes of a battery induce the generation of Mn oxides and oxyhydroxides such as Mn_3O_4 (hausmannite) as well as various polymorphs of MnOOH. Their appearance seems to play a major role in the battery efficiency and cyclability. Comprehensive knowledge of the mechanisms involved in the battery operation as well as the identification of the Mn compounds involved are of great importance to develop novel batteries with improved performance.

The design of well-defined manganese oxides and oxyhydroxides was investigated by ACG. Stable and crystalline nanowires and nanorod arrays of γ-MnOOH (manganite) of various textures were grown onto polycrystalline, single crystalline and amorphous substrates such as polypropylene, silicon wafers, and glass (Figure 16). In addition, manganese oxide nanocomposites consisting of manganite and hausmannite were generated by careful consideration of the Mn(II) and Mn(III) chemistry, which involved ligand and crystal-field stabilizations as well as controlled disproportionation reactions in solutions and at interfaces. Figure 17 shows electron microscopy images of some achievements. Such materials are currently under scrutiny to reach better fundamental understanding of their crystallographic relationships [115] as well as to develop novel materials for energy storage and conversion.

3.7 3-D arrays of anisotropic zinc oxide nano and microparticulates

Zinc oxide is an important large band gap II–VI semiconductor extensively studied for its electrical [116–119], optoelectronic [120–123], photoelectrochemical [124–126], and catalytic properties [127–130]. Recently, aligned and ordered 1-D nanorods of ZnO have shown their great potential for nanolaser applications [131]. The thermodynamically stable crystallographic phase of zinc oxide is wurtzite and occurs as the mineral Zincite (although scarcely as natural single crystal). Its ionic and polar structure can be described as hexagonal close packing (HCP) of oxygen and zinc atoms in point group *3m* and space group $P6_3mc$ with zinc atoms in tetrahedral sites. The occupancy of four of the eight tetrahedral sites of HCP arrays controls the structure. The crystal habit consists of a basal polar plane $(00\bar{1})$ and two types of low-index faces consisting of non-polar $(\bar{1}00)$ face (and C_{6v} symmetric ones) and tetrahedron corner-exposed polar (001) face (Figure 18). The 'low-symmetry' non-polar faces with 3-fold coordinated atoms are the most stables ones. The wurtzite structure has two specific characteristics that can be used to generate highly ordered materials. First, there is no center of inversion and therefore an inherent

asymmetry along the c-axis is present allowing the growth of anisotropic morphology. Such a structural characteristic is used to create three-dimensional array of highly oriented nanorod and microrod array of ZnO. Second, the structural surface metastability of the polar surface is used to design the corresponding highly oriented hollow structure by chemical dissolution of such faces. Due to the crystal symmetry and related face velocities, the common crystal habit of ZnO is a c-elongated hexagon.

Figure 16 SEM and TEM images of various crystalline Manganite nanorods and nanowire arrays grown by ACG onto polypropylene substrates

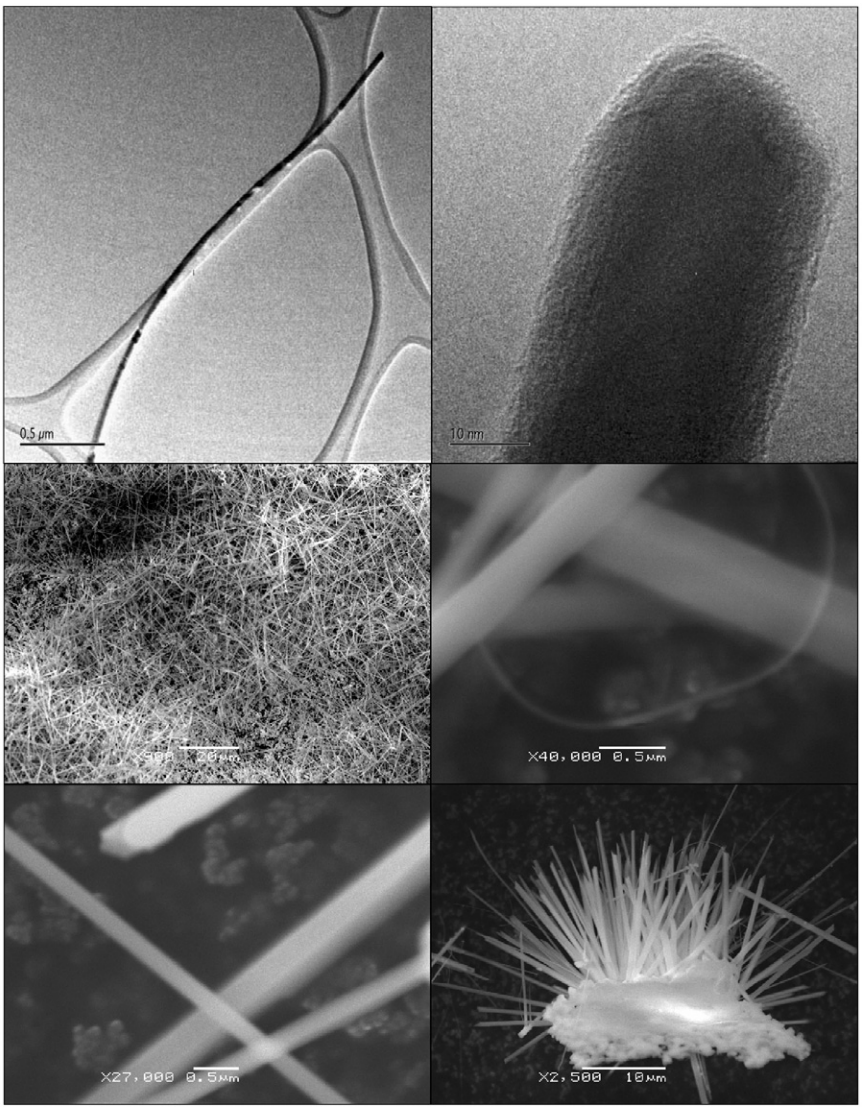

Figure 17 SEM and TEM images of Manganite-Hausmannite nanocomposites consisting of Mn_3O_4 nanoparticles grown onto γ-MnOOH nanorods

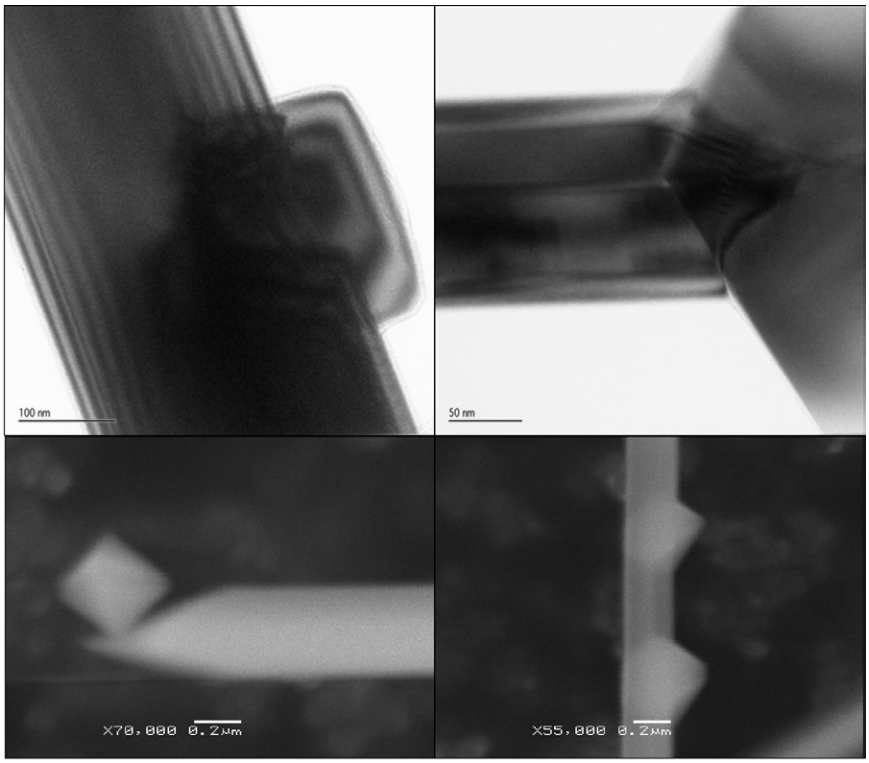

Due to the very low tendency of divalent metal ions to precipitate in aqueous solution by hydrolysis-condensation in neutral or acidic medium (compared to metal ions with higher oxidation state such as Fe^{3+} or Cr^{3+}), the synthesis was conducted by ACG and involved the aqueous thermal decomposition of Zn^{2+} amino-complex and the subsequent nucleation and growth of their crystalline oxide below 100°C. Highly oriented arrays of ZnO hexagonal microrods [132] and nanorods [133] were obtained (Figures 18 and 19). While the width of the rods is set by the precursors concentration and adjustable over an order of magnitude, ca. 1–2 μm at 0.1 M for the microrods and 100–200 nm at 0.01 M for the nanorods, their length may be experimentally tailored over two orders of magnitude to any required dimension up to 10 μm by adjusting the synthesis time. The growth rate can be as high as 1 μm per hour at 95°C for the microrods.

3-D array of hollow microrods of ZnO can be generated by taking advantage of the structural metastability of the materials and the use of a precipitation and ageing medium which utilizes the surface metastability of the top polar faces. The synthesis is a one-step, template-free, simple and cheap, aqueous synthesis which involved the aqueous thermal decomposition of Zn^{2+} amino-complex over an extended period of 48 h [134]. Such extended period of ageing was necessary to allow the growth of ZnO rods and to complete the preferential chemical dissolution of their top polar faces. Aligned single-crystalline hexagonal tubes of typically 1–2 μm in diameter and up to 10 μm in length with well-defined crystallographic faces are grown, along the [001] direction, in a

perpendicular fashion onto the substrates and are arranged in very large uniform arrays (Figure 19). Such highly porous and highly oriented well-defined microstructure was developed for dye-sensitized photovoltaic cells as well as for chemical and gas sensors. In addition, such oriented porous and crystalline structure may be utilized as a template to create nanocomposite materials with preferential orientations.

Figure 18 Crystal habit of zincite ZnO rods/tubes and SEM images of 3-D arrays of crystalline ZnO anisotropic microparticulates of various orientations and morphologies grown by ACG onto various substrates

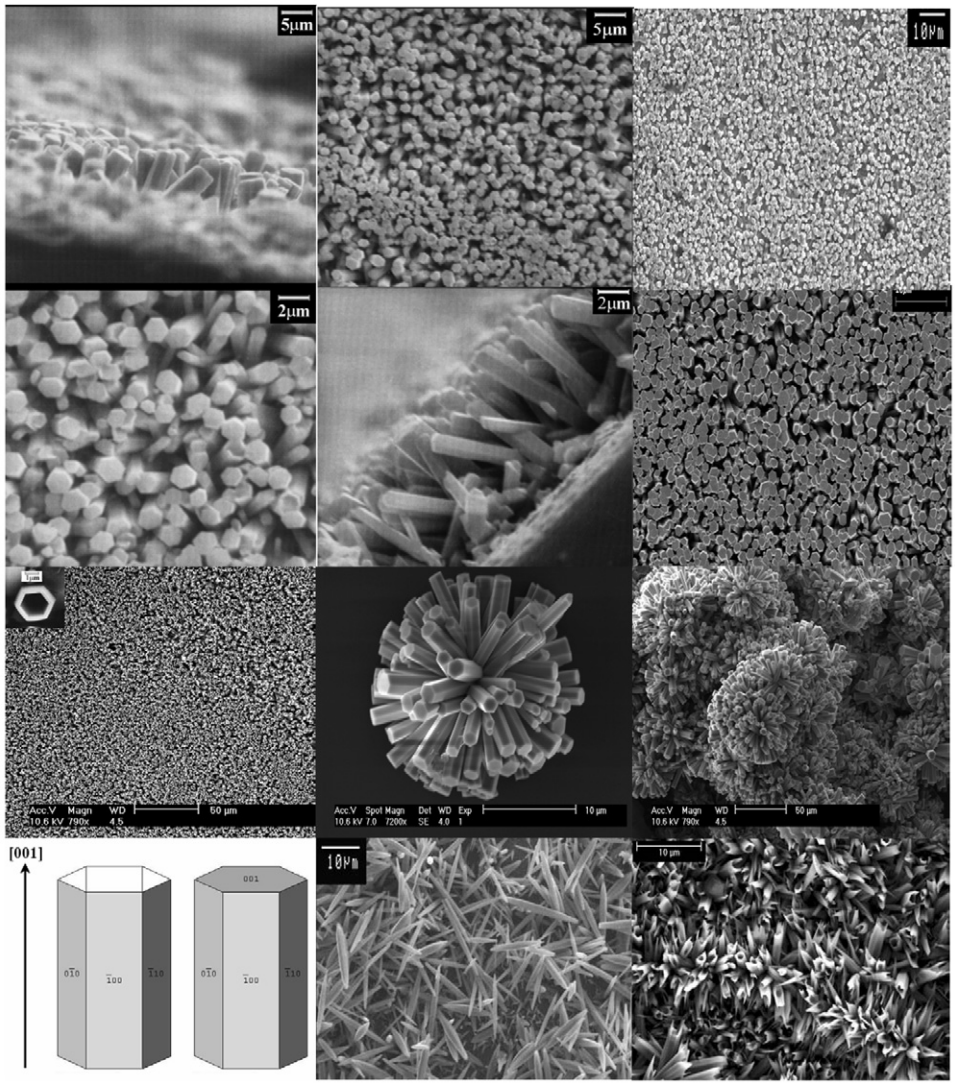

Nanowires of ZnO with narrow diameter (below 100 nm) can be generated by ACG [133], although their ordered 3-D growth onto substrates remains problematic. Figure 20 summarizes some achievements in ZnO nanowires of narrow diameters grown on Si wafers at low temperature. Such nanowires have been developed to enable the in-depth

electronic structure investigation, that is, to probe quantum confinement effects in such materials as well as demonstrating the effects of the scale law on physical and structural properties of such important II–VI semiconductor.

Figure 19 SEM images of 3-D arrays of crystalline ZnO anisotropic nanoparticulates of various orientations and textures grown by ACG onto various substrates

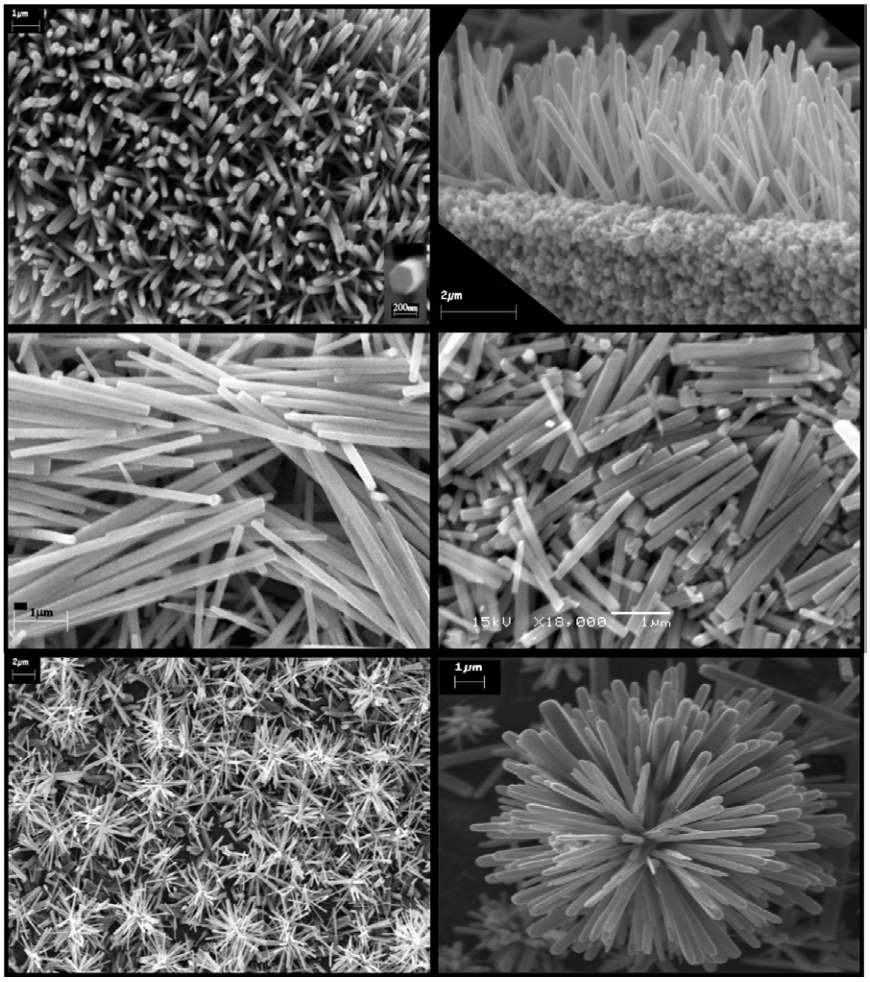

3.8 3-D arrays of isotropic ruthenium oxide nanoparticulates

Group VIII metal and metal oxides (e.g. RuO_2, IrO_2) are extensively studied for research and development of electrocatalysts for chlorine, oxygen or hydrogen evolution for fundamental and applied purposes. It represents important energetic, economic, and environmental issues of the chemical industry. However, their stability against corrosion and passivation at high current density and applied bias is problematic. In the last decade, mixed oxide materials from group VIII and group IV and V were investigated to improve

the corrosion resistance of electrodes. However, the electrocatalytic activity seemed to depend strongly on the chemical composition of the material and was very sensitive to the contamination induced by the synthetic processes. Further technological improvements will contribute to achieve more reliable and durable electrode materials. However, as far as the performance is concerned, the most significant breakthrough will most probably occur from a better fundamental knowledge of the correlations between surface compositions and electronic structure of the electrode materials and their electrocatalytic activities. Moreover, better general understandings of the mechanisms and kinetics of the electro-oxidation processes will certainly help reaching such goals. A key to obtain such crucial information will originate from materials science development of novel and smart nanomaterials. To fulfil the needs of stability and performance and to study the effect of morphology, high surface area, and porosity on the electrocatalytic activity, new type of thermodynamically stable and porous electrode materials have to be developed.

Figure 20 SEM and TEM images of various crystalline ZnO nanowire arrays grown by ACG onto silicon wafers

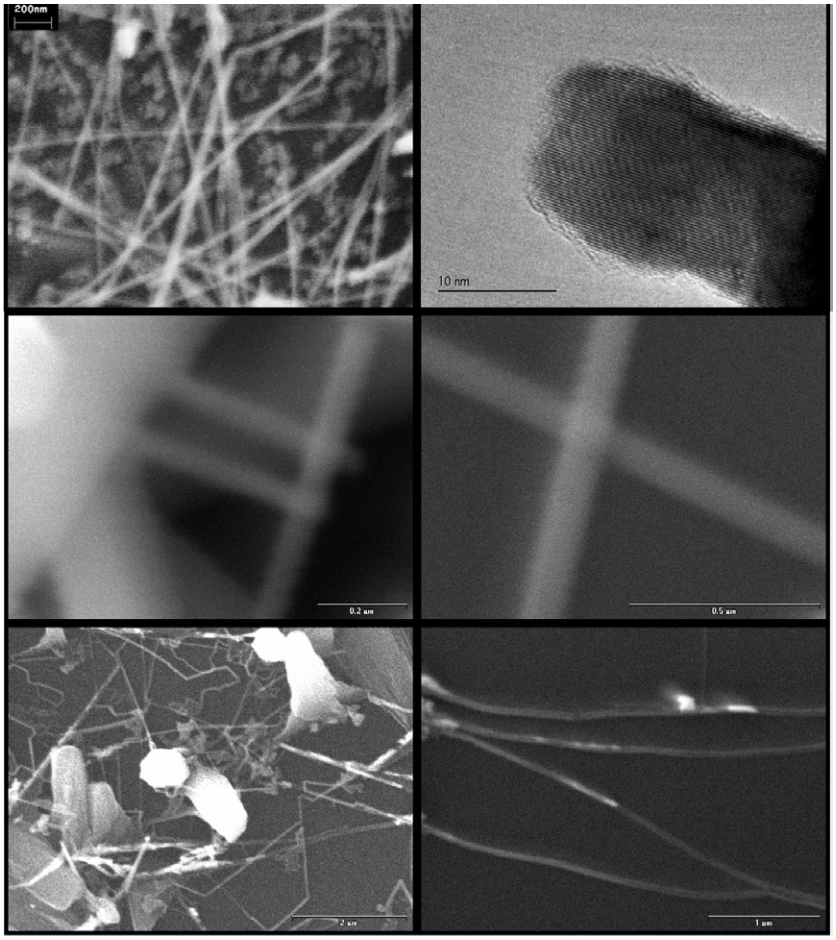

The approach to nanomaterials design of group VIII is somehow different from the common trivalent 3d transition metal cations such as Fe, Cr, or Al, due to the occurrence of disproportionation reactions. It is indeed typically the case of ruthenium, which Ru^{3+} precursors generate the formation of Ru^{4+} (as RuO_2) and Ru^0 (Ru metal) in solution and in solid state. The concomitant presence of ruthenium metal and its dioxide is a major drawback for electrocatalysis. Indeed, while the dioxide of ruthenium is highly resistant to chemical and electrochemical corrosion, ruthenium metal is not. The corroding current under anodic polarization can be so high that the overall electrocatalytic activity is severely reduced. Hitherto, the formation of RuO_2 thin films consisted of high temperature annealing in oxygen atmosphere of concentrated $RuCl_3$ solutions sprayed onto a substrate. The purpose was to oxidize Ru into RuO_2 to compensate for the uncontrolled disproportionation reaction. However, such approach yielded very compact electrodes of low specific surface area and poor activity.

Our strategy is to take advantage of such reaction [135]. Indeed, by creating a spatial segregation of the metal and metal oxide phases, the generation of an oxide-on-its-metal electrode consisting of a RuO_2 layer grown on a Ru layer could be achieved. In addition, by growing such layers with nanoparticles arranged in a highly porous layer on chemically resistant substrate, a novel and very suitable electrode for electrocatalysis (chlorine or oxygen evolution) can be fabricated. An attempt to achieve such ambitious goal was conducted by creating novel electrode materials consisting of thin films of hydrated nanostructured ruthenium dioxide supported on nanostructured ruthenium. Such purpose-built nanocomposite was grown by ACG on chemically inert and flexible substrate such as Teflon (FEP) or polypropylene (PP) (Figure 21).

Figure 21 SEM and TEM images of a purpose-built porous ruthenium oxide/ruthenium nano-composite thin film grown onto Teflon FEP

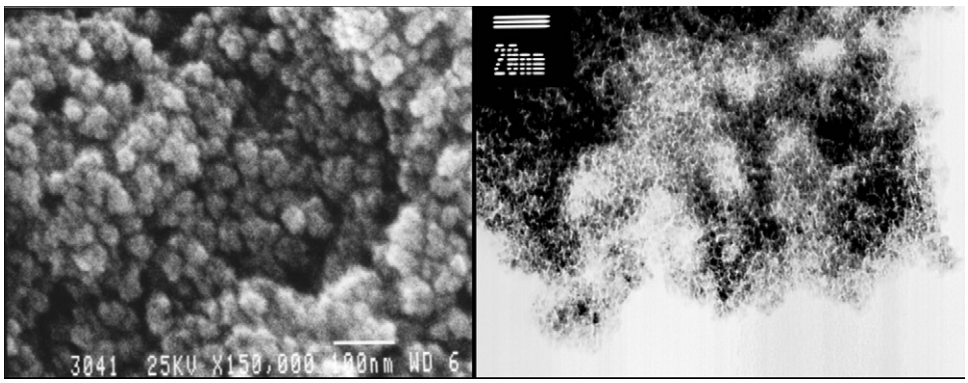

In addition to the high electrocatalytic activity, ruthenium dioxide is a well-known supercapacitor [136–138]. Indeed, its capacitance is one of the highest ever reported. In combination with its very good thermal and chemical stability, it represents one of the best materials for supercapacitors. Unfortunately, its cost is prohibitive and basically, no industrial development has been carried out. However, by designing it at nanoscale with a high porosity, the mass of the ruthenium precursors is considerably reduced and so is its cost. Consequently, high-performance stable electrode materials of high capacitance for supercapacitors and electrocatalysts may be generated at relatively low-cost. Figure 22 shows the cyclic voltammograms recorded in aqueous solution of low concentrated

sulfuric acid (0.5 M) is featureless, which reveals a high and pure double-layer capacitance as well as a very good cyclability, considering that the thin films are gown on Teflon (FEP) substrates.

Figure 22 Cyclic voltammograms in 0.5 M H_2SO_4 aqueous solution of the purpose-built highly porous ruthenium oxide/ruthenium nanocomposite thin films grown onto Teflon FEP by ACG: (left) high capacitance (20 scans at a scan rate of 20 mV/s) and (right) good stability and cyclability (100 scans at a scan rate of 100 mV/s)

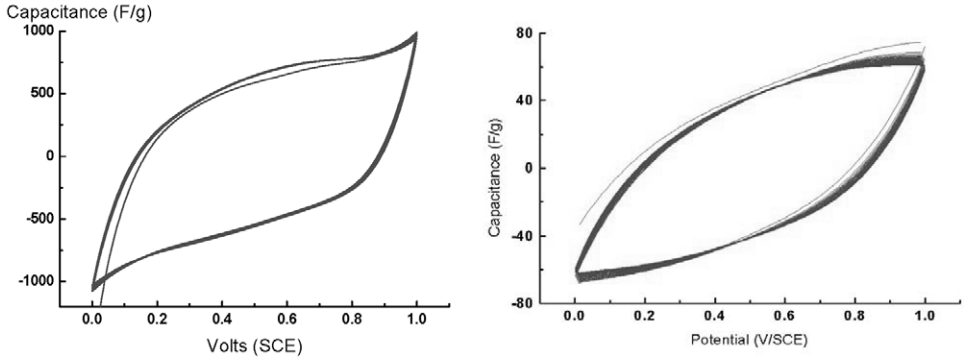

Alternatively, the synthesis of doped or mixed ruthenium oxide with other metal oxides has been investigated in the literature [139–141] in an attempt to reduce the ruthenium content and so, the effective cost of future devices.

3.9 3-D arrays of bio-metal oxide nanocomposites

A new era of nanomaterials is emerging which combines the unique properties of nanostructured materials, the wide variety of physical properties of metal oxides and bio-active materials such as DNA, peptides, enzymes, antibodies, or bacteria. Linking such important classes of materials is aiming to develop advanced bio-nanomaterials and novel nano-biosensors. Such composites should exhibit a higher sensitivity due to very high surface area of the nanomaterials, a better selectivity and specificity due to well-designed morphology, and a greater functionality due to the ability to grow selectively on various types of surfaces. In addition, such advanced devices may show a faster response time and a better reliability and durability.

Indeed, ACG can generate *purpose-built* hydrated nanomaterials that can provide very suitable templates for the growth of advanced nanocomposite bio-materials. Our approach to create such novel and designed bio-nanocomposite materials is to fabricate selected metal oxide particulate thin films with the appropriate crystal structure, texture, and composition. The following strategy is to tune their surface charge density and interfacial properties to induce preferred chemisorptions and growth patterns for the bioactive compounds. Such ability was demonstrated by the design of a novel metal oxide bio-nanocomposite thin film consisting of antimicrobial peptides (e.g. bola-amphiphile) assembled onto hydrated semiconducting metal oxide nanomaterials [142]. The results are shown in Figure 23. Stable and highly porous 3-D nanostructures of large physical area are obtained on many types of substrates.

Due to the enhanced flexibility and bio-compatibility of the ACG synthesis method and the general concepts of interfacial thermodynamic control of nucleation and growth, very promising results are foreseen for the development of advanced nanocomposite bio-sensors.

Figure 23 SEM images of a metal oxide-bioactive nanocomposite materials consisting of highly porous 3-D arrays of self-assembled antimicrobial peptides onto a purpose-built metal oxide nanomaterial grown by ACG

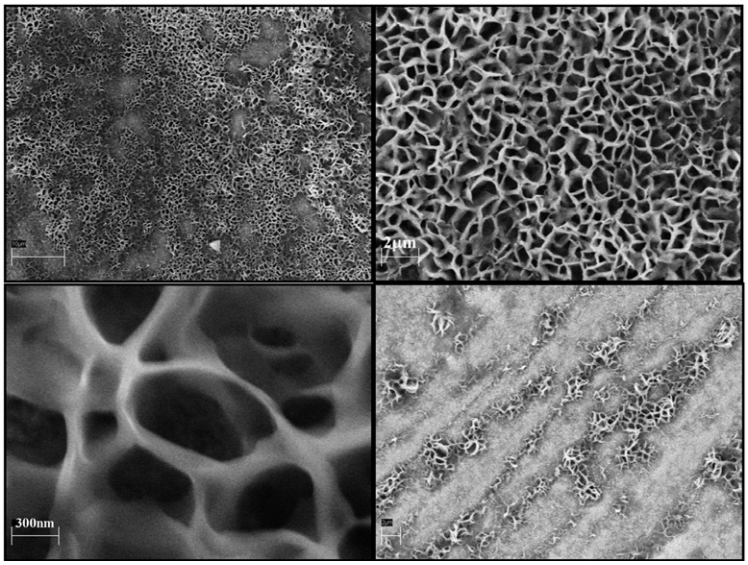

4 Electronic structure

Better fundamental knowledge of the electronic structure as well as the structural and physical properties of nanomaterials is required to unfold the full potential of their unique properties and applications. The fabrication of large arrays of nano-, meso-, and micro-crystallites with well-controlled size and orientation, and well-defined morphology onto various substrates enables to perform experiments on real devices (polycrystalline) by UHV techniques such as X-ray absorption, emission, and scattering spectroscopies at synchrotron radiation facilities [143]. Therefore, the influence of such parameters can be probed and demonstrated. The comparison to studies carried out on single-crystals as well as quantum calculations and molecular dynamics simulations performed on periodic crystals would contribute to reach a better comprehensive fundamental understanding of the difference and similitude of these two classes of crystalline materials. Consequently, a direct feedback between experimental and calculated data should contribute to obtain an in-depth comprehensive knowledge of the physical, chemical, and structural properties at nanoscale (compared to bulk properties).

ACG has enabled to generate metal oxide nanomaterials with controlled size, surface morphology, orientation, composition, porosity, and overall film texture and allowed to investigate its influence as well as following a trend in oxidation states, electronic configuration, and crystal structure for nanostructured transition metal oxides. Thus, current metal oxide-based nanodevices could be improved and optimized and novel ones

could be created based on such knowledge. As an example, to illustrate and demonstrate the importance of the rational fabrication of oriented and well-defined nano/microparticulate thin films, the study of the effects of orientation and morphology, as well as the influence of the size, on the electronic structure on transition metal oxide particulate thin films was carried out by X-ray absorption spectroscopy (XAS) at the Advanced Light Source (ALS) synchrotron radiation facility at Lawrence Berkeley National Laboratory (LBNL). Besides the high resolution and high flux, the major characteristics of X-ray spectroscopic measurements at synchrotron facilities are: the atomic selectivity due to the transitions involving core levels as well as the orbital (and symmetry) selectivity due to the dipole selection rules and the polarization of X-ray sources.

4.1 Orbital symmetry

The study of the effect of orientations and morphology on the electronic structure of ZnO was carried out by polarization-dependent X-ray absorption spectroscopy. The experiments were conducted on two different wurtzite ZnO polycrystalline samples, i.e. isotropic and anisotropic. The first sample consisted of a 3-D array of perpendicularly oriented rods and the second sample consisted of a 3-D array of monodispersed spherical particles.

The O K-edge XAS spectra of the anisotropic and isotropic arrays recorded at grazing and normal incidence with a spectral resolution of 0.2 eV are displayed in Figure 24 (top graphs).Variations in spectral shape were observed up to 30 eV above the absorption threshold. The resolved absorption features are indicated as a_1 to a_8. Up to feature a1, no polarization dependence is observed in the X-ray absorption spectra for either sample. However, for the ZnO microrods (bottom spectra), strong anisotropic effects were observed at higher photon energies. At grazing incidence ($\theta = 10°$), the excitation to the state along the c-axis of the wurtzite structure is enhanced and the absorption features a_3, a_5, and a_8 were stronger, At normal incidence ($\theta = 90°$), the excitation to the in-plane state is enhanced and the absorption features a_2, a_4, and a_7 were stronger, No significant change was observed for the isotropic samples. However, all the absorption features were averaged out and observed in the XAS spectra measured with either geometrical detection. To fully demonstrate the influence of the oxygen orbital symmetry and its contribution to the conduction band of ZnO, full-potential calculations of orbital-resolved X-ray absorption of a periodic crystal of ZnO were carried out. An excellent agreement between the calculated density of states and the experimental data was obtained (Figure 24, bottom graphs). As a result, the contribution of the symmetry of oxygen *p* orbitals to the conduction band and bulk properties of ZnO was clearly probed and demonstrated [144]. Such in-depth fundamental knowledge is of great importance for the development of better II–VI semiconductor optoelectronic devices based on ZnO.

4.2 Quantum confinement

The study of the effects of quantum size on the chemical/physical properties and the electronic structure of nanostructured materials is of great interest for a better understanding of their properties. By following the fundamental and experimental concepts exposed in this review, nanoparticulate thin films of titanium oxide were fabricated with well-controlled nanoparticle sizes. Such designed nanomaterials allowed to illustrate the influence of the decrease of the nanoparticle size on the density of unoccupied states of the conduction band of TiO_2.

Figure 24 O K-edge polarization dependent X-ray absorption spectra (XAS) of crystalline 3-D arrays of ZnO of isotropic and oriented anisotropic morphology (top). The inset illustrates the experimental XAS geometry, where *a*, *b* axes defined the sample-surface plane, *c* axis was along the growth direction of the ZnO rods, *E* is the polarization of the incoming photons, and θ represents the incident angle to the sample surface: 10° ($E \parallel c$, lines) and 90° ($E \perp c$, dots). The bottom graph displays the experimental (top) and calculated (bottom) O K-edge XAS spectra of ZnO as a function of the polarization angle. The calculated XAS spectra feature the partial density of states (DOS) and the transition probability to O $2p_{x+y}$ and $2p_z$ states with a Lorentzian broadening equivalent to the experimental spectral resolution (0.2 eV) [144]

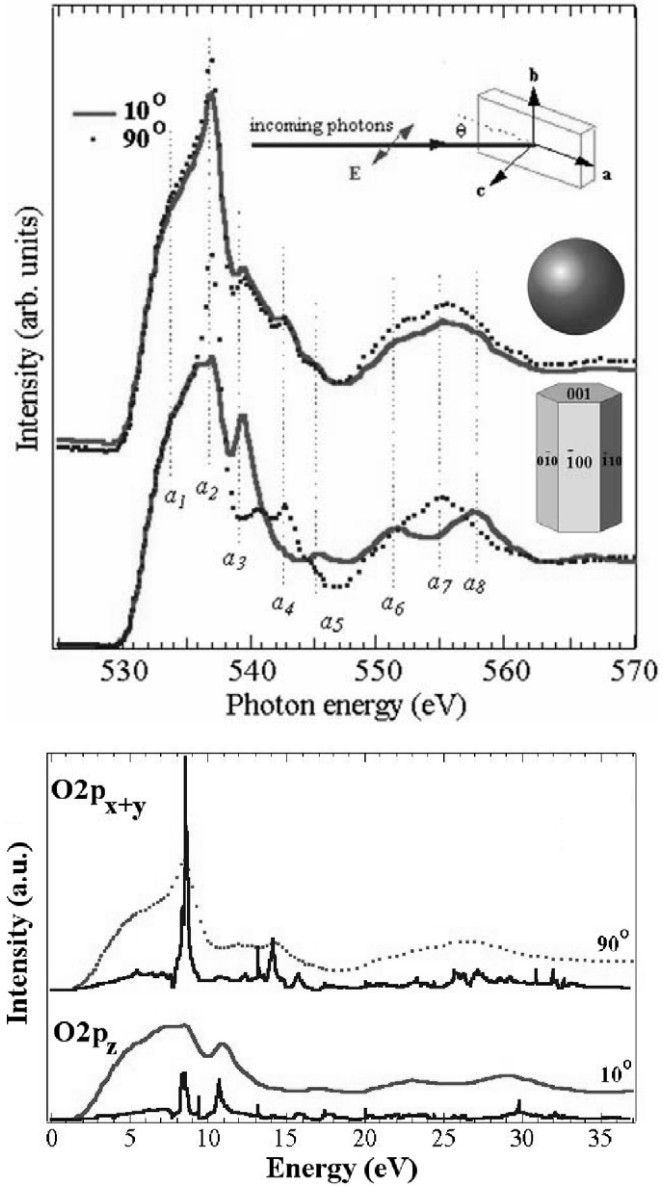

Figure 25 shows the XAS spectra at O K-edge of isotropic nanoparticulate thin films of anatase TiO_2 of different average spherical particle sizes of narrow distributions. The spectra can be divided into two distinct regions above and below the ionisation threshold (~536 eV). The first region is attributed to oxygen 2*p* hybridised with predominantly Ti 3*d* states [145–147]. The second region (above the threshold) is attributed to oxygen 2*p* character hybridized with Ti 4*s* and 4*p* states [148]. Such large energy spread (some 15 eV) of oxygen 2*p* states is an indication of strong covalency in TiO_2. In a purely ionic model, oxygen would have the configuration $1s^2 2s^2 2p^6$ and the $1s \rightarrow 2p$ channel would be closed in the X-ray absorption process. Covalency reduces the number of filled states of O 2*p* character, so that the intensity of the O 1*s* signal at the threshold is related to the degree of covalency [149]. The decrease in intensity of the first-region bands, relative to the second-region bands is consistent with observations reported in the literature for O 1*s* XAS studies of the transition-metal series [145,150]. This is understood by the decrease in number of unoccupied 3*d* states available for mixing with O 2*p* states.

Figure 25 O K-edge X-ray absorption spectra of anatase TiO_2 isotropic nanoparticulate thin films consisting of spherical nanoparticles of controlled sizes. The spectra were recorded in electron yield mode with a spectral resolution of 0.2 eV

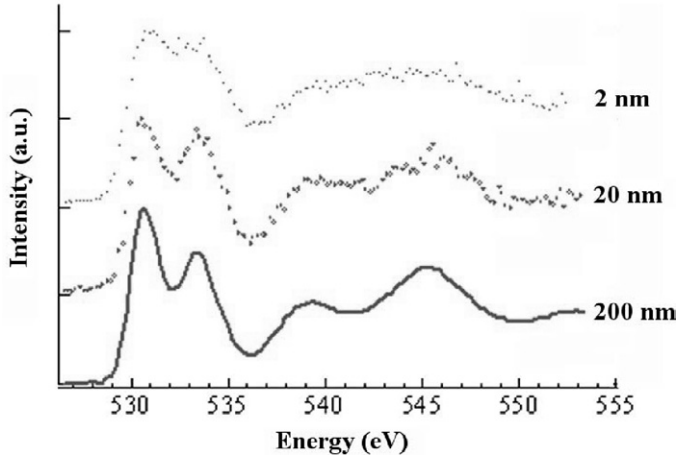

For nanoparticulate samples, the main effect of the decrease of the particle size is to increase the surface-to-volume ratio, which results in a tremendous increase of the amount of atoms at the interface. This contributes to an overall reduction of the symmetry due to the surface non-stoichiometry. In addition, decreasing the nanoparticle size induces the generation of unoccupied bandgap states in large bandgap semiconductors. Due to the general contracted (core-like) nature and narrow bandwidth of the 3*d* orbitals, the hybridisation of O 2*p* with Ti 4*s* orbitals is expected to be of substantial importance due to the extended radial distribution of *s* orbitals (compare to *d* orbitals) and the general lowering of the octahedral symmetry. As a result, a significant broadening of the second region of the O 1*s* spectra is expected as the nanoparticle size decreases and reaches the quantum confinement regime. An excellent agreement is obtained with the XAS experiments and very promising results are expected for mapping the electronic structure of transition metal oxides in quantum regime. Indeed, the knowledge of the orbital

character of localized band gap states is of great importance to understand the unique optical and photoelectrochemical properties of semiconductor nanomaterials. Thus, first-principal ab-initio calculations were carried out on periodic crystals of anatase structure. The density of states and the absorption spectra at O K-edge were calculated and compared to the experimental data. An excellent agreement was found between the simulation and experimental absorption spectra as well as additional evidence of the quantum effects on the electronic structure of TiO_2 [151]. Further experimental and theoretical studies are currently in progress to account for the optical properties and electronic structure of TiO_2 nanoparticulate thin films under electrochemical bias in acidic medium [152].

5 Conclusions

The rational fabrication of advanced nanomaterials was demonstrated by the experimental monitoring of the interfacial thermodynamics and kinetics of nucleation, growth, and ageing processes. Such ability is reached by the chemical and electrostatic control of the interfacial free energy as predicted by a model based on the Gibbs adsorption equation. Aqueous chemical growth exploits such concepts and enables the modelling, the design, and the fabrication of functional purpose-built metal oxide thin films with well-defined textures onto various substrates at low temperature and at low cost. Therefore, the economical large-scale manufacturing of a new generation of smart metal oxide materials with extended functionality and surface nanoengineered morphology is readily available. Such purpose-built materials should contribute to develop novel and optimised devices for high technological applications, as well as biological and medical related ones. They also constitute well-defined samples that enable reaching better fundamental knowledge and understanding of nanostructured materials and their fascinating physical, chemical, and structural properties as well as their unique electronic structure.

Acknowledgements

The work described in this article was supported by the Pierre & Marie Curie University in Paris, the Swedish material research consortium on clusters and ultrafine particles (NUTEK-SSF), the departments of Physics and Physical Chemistry at Uppsala University, the Gustavsson foundation for research in Natural Science and Medicine, and the Swedish International Development & Cooperation Agency (SIDA). This work was also supported in part by the US Department of Energy, Director, Office of Science, Office of Basic Energy Sciences, Chemical Sciences Division at Lawrence Berkeley National Laboratory (LBNL) under contract No. DE-AC03-76SF00098, and by the Texas Materials Institute under Welch grant F-1524.

References

1 Regis, E. and Chimsky, M. (1996) *Nano: The Emerging Science of Nanotechnology,* Little, Brown & Co.

2 Wilson, M. (2002) in Simmons, M., Smith, G. and Kannangara, K. (Eds.) *Nanotechnology: Basic Science and Emerging Technologies,* CRC.

3 Nalwa, H.S. (Ed.) (2003) Encyclopedia of Nanoscience and Nanotechnology, ASP.

4 Bard, A.J. (1994) Integrated Chemical Systems: A Chemical Approach to Nanotechnology, Wiley.

5 Klabunde, K.J. (Ed.) (2001) *Nanoscale materials in chemistry*, Wiley.

6 Robinson, D. (1996) in Coombs, R. (Ed.) *Nanotechnology in Medicine and the Biosciences*, Gordon & Breach.

7 Hoch, H.C., Jelinski, L.W. and Craighead, H.G. (Eds.) (1996) Nanofabrication and Biosystems: Integrating Materials Science, Engineering, and Biology, Cambridge University Press.

8 Freitas Jr., R.A. (1999) *Nanomedicine*, Landes Bioscience.

9 Mosznert, N. (2004) *Int. J. Nanotechnol*., Vol. 1, Nos. 1/2, pp.130–156.

10 Hochella, M.F. (2002) Earth *Planet. Sci. Lett.*, Vol. 203, pp.593–605.

11 Waychunas, G. (2004) *Int. J. Nanotechnol*., Vol. 1, No. 3, (To be published).

12 Bhushan, B. (Ed.) (2001) Fundamentals of Tribology and Bridging the Gap between the Macro and Micro/Nanoscales, Kluwer.

13 Roco, M.C. and Bainbridge, W.S. (Eds.) (2002) *Societal Implications of Nanoscience and Nanotechnology*, Kluwer.

14 Edelstein, A.S. and Cammarata, R.C. (Eds.) (1998) *Nanomaterials: synthesis, properties, and application*s, IOP.

15 Hofmann, H., Rahman, Z. and Schubert, U. (Eds.) (2002) *Nanostructured Materials*, Springer-Verlag.

16 DiNardo, N.J. (Ed.) (1994) Nanoscale Characterization of Surfaces and Interface, VCH.

17 Gardener, J.W. and Hingle, H.T. (Eds.) (1991) *From Instrumentation to Nanotechnology*, Gordon and Breach.

18 Wang, Z.L. (Ed.) (2000) Characterization of Nanophase Materials, Wiley.

19 Lieber, C.M. (1998) *Solid State Comm*., Vol. 107, No. 11, pp.607–616.

20 Huang, Y., Duan, X., Wei, Q. and Lieber, C.M. (2001) *Science*, Vol. 291, No. 5504, pp.630–633.

21 Peng, X., Manna, L., Yang, W., Wickham, J., Scher, E., Kadavanich, A. and Alivisatos, A.P. (2000) *Nature*, Vol. 404, pp.59–61.

22 Zarur, A.J. and Ying, J.Y. (2000) *Nature*, Vol. 403, pp.65–67.

23 Martin, C.R. (1996) *Chem. Mater.*, Vol. 8, pp.1739–1746.

24 Xia, Y. Rogers, J.A. Paul, K.E. and Whitesides, G. M. (1999) *Chem. Rev*., Vol. 99,No. 7, pp.1823–1848.

25 Liu, R. Vertegel, A. Bohannan, E.W. Sorenson, T.A. Switzer, J.A. (2001) *Chem. Mater.*, Vol. 13, No. 2, pp.508–512.

26 Adachi, M., Harada, T. and Harada, M. (1999) *Langmuir*, Vol. 15, No. 21, pp.7097–7100.

27 Kasuga, T., Hiramatsu, M., Hoson, A., Sekino, T. and Niihara, K. (1998) *Langmuir* Vol. 14, No. 12, pp.3160–3163.

28 Whangbo, M.-H. and Koo, H.-J. (2000) *Solid State Comm.*, Vol. 115, pp.675–678.

29 Satishkumar, B.C., Govindaraj, A., Vogl, E.M., Basumallick, L. and Rao, C.N.R. (1997) *J. Mater. Res.*, Vol. 12, No. 3, pp.604–606.

30 Niederberger, M., Muhr, H.J., Krumeich, F., Bieri, F., Gunther, D. and Nesper, R. (2000) *Chem. Mater.*, Vol. 12, No. 7, pp.(1995–2000).

31 Nanai, L., George, T.F. (1997) *J. Mater. Res.*, Vol. 12, No. 1, pp.283–284.

32 Hoyer, P. (1996) *Langmuir*, Vol. 12, No. 6, pp.1411–1413.

33 Cepak, V.M., Hulteen, J.C., Che, G., Jirage, K.B, Lakshmi, B.B., Fischer, E.R. and Martin, C.R. (1997) *Chem. Mater.*, Vol. 9, No. 5, pp.1065–1067.

34 Terrones, M., Grobert, N., Olivares, J., Zhang, J.P., Terrones, H., Kordatos, K., Hsu, W.K., Hare, J.P., Townsend, P.D., Prassides, K., Cheetham, A.K., Kroto, H.W. and Walton, D.R.M. (1997) *Nature*, Vol. 388, pp.52–55.

35 Dai, H., Kong, J., Zhou, C., Franklin, N., Tombler, T., Cassell, A., Fan, S. and Chapline, M. (1999), *J. Phys. Chem. B*, Vol. 103, No. 51, pp.11246–11255.

36 Vayssieres, L., Hagfeldt, A. and Lindquist, S-E. (2000) *Pure Appl. Chem.*, Vol. 72, No. 1/2, pp.47–52.

37 (a) Vayssieres, L. (1995) Ph.D. Thesis, Université Pierre et Marie Curie, Paris, pp.1–145. (b) Vayssieres, L. (2004) *Int. J. Nanotechnol.*, Vol. 1, No. 3, (to be published).

38 Aveyard, R. (1987) *Chem. Ind.*, Vol. 14, pp.474–478.

39 Vayssieres, L. (2000) IUPAC/UNESCO Virtual Teaching Encyclopedia on Macromolecules and Materials Science on CD-ROM, pp.3–32.

40 Vayssieres, L., Chaneac, C., Tronc, E. and Jolivet, J.P. (1998) *J. Colloid Interface Sci.*, Vol. 205, No. 2, pp.205–212.

41 Vayssieres, L., Hagfeldt, A. and Lindquist, S-E *PCT application WO9935312*, pp.1–49.

42 Baes, C.F. and Mesmer, R.E. (1976) *The Hydrolysis of Cations* ,Wiley.

43 Vayssieres, L. (To be published).

44 Weckhuysen, B. and Schoonheydt, R. (1999) *Catalysis Today*, Vol. 51, p.223.

45 de Rossi, S., Casaletto, M.P., Ferraris, G., Cimino, A. and Minelli, G. (1998) *Appl. Catal. A*, Vol. 167, p.257.

46 Wang, S., Murata, K., Hayakawa, T., Hamakawa, S. and Suzuki, K. (2000) *Appl. Cata. A*, Vol. 196, p.1.

47 Cho, B., Choi, E., Chung, S., Kim, K., Kang, T., Park, C. and Kim, B. (1999) *Surf. Sci.*, Vol. 439, L799.

48 Berdahl, P. (1995) *Trans. ASME J. Heat Transfer*, Vol. 117, p.355.

49 Hornreich, R.M. and Shtrikman, S. (1968) *Phys Rev.*, Vol. 171, No. 3, p.1065.

50 Krichvtsov, B.B., Pavlov, V., Pisarev, R.V. and Gridnev, V. (1993) *J. Phys.: Condens. Matter*, Vol. 5, p.8233.

51 Kouvo, O. and Vuorelainen, Y. (1958) *Am. Miner.*, Vol. 43, p.1098.

52 Catti, M., Sandrone, G., Valerio, G. and Dovesi, R. (1996) *J. Phys. Chem. Solids*, Vol. 57, No. 11, p.1735.

53 Latacz, Z. (2001) *J. Alloys Comp*., Vol. 316, p.18.

54 Brown, W.F., Shtrikman, S. and Treves, D. (1963) *J. Appl. Phys.*, Vol. 34, p.1233.

55 Graham, E.B. and Raab, R.E. (1994) *J. Phys.: Condens. Matter*, Vol. 6, p.6725.

56 Graham, E.B. and Raab, R.E. (1992) *Phil. Mag. B*, Vol. 66, p.269.

57 Tanabe, Y., Muto, M. and Hanamura, E. (1997) *Solid State Comm*., Vol. 102, No. 9, p.643.

58 Costa, M.F.M., Teixeira, V. and Nunes, C. (1999) *Proc. SPIE*, Vol. 3789, p.140.

59 Coey, J.M., Berkowitz, A.E., Balcells, L., Putris, F. and Barry, A. (1998) *Phys Rev. Lett.,* Vol. 80, p.3815.

60 Balasubramanian, M. and Melendres, C.A. (1999) *Electrochimica Acta*, Vol. 44, 2941.

61 Hones, P., Levy, F. and Randall, N.X. (1999) *J. Mater. Res.*, Vol. 14, No. 9, p.3623.

62 Zhang, L., Khun, M. and Diebold, U. (1997) *Surf Sci.*, Vol. 375, p.1.

63 Chevalier, S., Bonnet, G. and Largin, J.P. (2000) *Appl. Surf. Sci.*, Vol. 167, p.125.

64 Dolgaev, S.I., Kirichenko, N.A. and Shafeev, G.A. (1999) *Appl. Surf. Sci.*, Vol. 138–139, p.449.

65 Vayssieres, L. and Manthiram, A. (2003) *J. Phys. Chem. B*, Vol. 107, No. 12, pp.2623–2625.

66 (a) McLure, D.S. (1963) *J. Chem. Phys.*, Vol. 38, No. 9, p.2289; (b) Kirby, E.R., Garwin, E.L., King, F.K. Nyaiesh, A.R. (1987) *J. Appl. Phys.*, Vol. 62, No. 4, p.1400; (c) Zhang, L.D., Mo, C.M., Cai, W.L. and Chen, G. (1997) *Nanostruct. Mater*., Vol. 9, p.563.

67 Sugano, S., Tanabe, Y. and Kamimura, H. (1970) *Multiplets of Transition-Metal ions in Crystals*, Academic Press.

68 Fiebig, M., Frohlich, D., Leute, S., Lottermoser, T., Pavlov, V. and Pisarev, R.V. (2001) *J. Magn. Magn. Mater.*, Vol. 226–230, p.961.

69 Fiebig, M., Frohlich, D., Krichevtsov, B.B. and Pisarev, R.V. (1994) *Phys. Rev. Lett*., Vol. 73, p.2127.

70 Cottam, M.G and Lockwood, D.J. (1986) *Light Scattering in Magnetic Solids*, Wiley.

71 Muthukumar, V.N., Valenti, R. and Gros, C. (1995) *Phys. Rev. Lett.*, Vol. 75, No. 14, p.2766.

72 Ando, M., Kadono, K., Haratu, M., Sakaguchi, T. and Miya, M. (1995) *Nature*, Vol. 374, No. 6523, p.625.

73 Cline, J.A., Rigos, A.A. and Arias, T.A. (2000) *J. Phys. Chem. B*, Vol. 104, p.6195.

74 Jambor, J.L. and Dutrizac, J.E. (1998) *Chem. Rev.*, Vol. 98, pp.2549–2585.

75 Stumn, W. and Morgan, J.J. (1996) *Aquatic Chemistry*, Wiley.

76 Winklemann, G., Van der helm, F. and Neidlans, J.B. (1987) *Iron transport in Microbes, Plants and Animals*, VCH.

77 Garvie, L.A.J. and Buseck, P.R. (1998) *Nature*, Vol. 396, pp.667–670.

78 Kostka, J.E., Haefele, E., Viehweger, R. and Stuck, J.W. (1999) *Environ. Sci. Technol.*, Vol. 33, pp.3127–3133.

79 Bao, H.M., Koch, P.L. and Hepple, R.P. (1998) *J. Sediment. Res.*, Vol. 68, No. 5, pp.727–738.

80 Ellwood, B.B., Petruso, K.M., Harrold, F.B. and Schuldenrein, D. (1997) *J. Archeological Sci.*, Vol. 24, pp.569–573.

81 Stumm, W. and Sulzberger, B. (1992) *Geochim. Cosmochim. Acta*, Vol. 56, No. 8, pp.3233–3257.

82 Kletetschka, G., Wasilewski, P. and Taylor, P. (2000) *Phys. Earth Planet. In.*, Vol. 119, pp.259–267.

83 Lovley, D.R. (1991) *Microbiol. Rev.*, Vol. 55, No. 2, pp.259–287.

84 Cornell, R.M. and Schwertmann, U. (1996) *The Iron Oxides*, VCH.

85 Morse, P.G. (1998) *Chem. Eng. News*, Vol. 76, No. 41, pp.42–62.

86 Tano, K., Öberg, E., Samskog, P.O. Monredon, T. and Broussaud, A. (1999) *Powder Technol.*, Vol. 105, pp.443–450.

87 Von Ropenack, A. (1986) in Dutrizac, J.E. and Monhemius, A.J. (Eds.): *Iron Control in Hydrometallurgy*, Ellis Horwood, pp.730–741.

88 Pestman, R., Koster, R.M., Boellaard, E., Van der Kraan, A.M. and Ponec, V. (1998) *J. Catal.*, Vol. 174, pp.142–152.

89 Lin, S.-S. and Gurol, M.D. (1998) *Environ. Sci. Technol*., Vol. 32, pp.1417–1423.

90 Zhang, Y., Ellison, J.E. and Cannon, J.C. (1997) *Ind. Eng. Chem. Res.*, Vol. 36, No. 5, pp.1948–1952.

91 Matsumoto, Y. (1996) *J. Solid State Chem.*, Vol. 126*,* pp.227–234.

92 Licht, S., Wang, B. and Ghosh, S. (1999) *Science*, Vol. 285, pp.139–1042.

93 Kellog, C.B. and Irikura, K.K. (1999) *J. Phys. Chem. A*, Vol. 103, No. 8, pp.1150–1159.

94 Oh, S.E., Cook, D.C. and Townsend, H.E. (1999) *Corrosion Sci.*, Vol. 41, pp.1687–1702.

95 Vayssieres, L., Beermann, N., Hagfeldt, A. and Lindquist, S.E. (2001) *Chem. Mater.*, Vol. 13, No. 2, pp.233–235.

96 Beermann, N., Vayssieres, L., Lindquist, S.E. and Hagfeldt, A. (2000) *J. Electrochem. Soc.* Vol. 147, No. 7, pp.2456–2461.

97 Lindgren, T., Wang, H., Bermann, N., Vayssieres, L., Hagfedlt, A. and Lindquist, S.E. (2002) *Solar Energy Mater. Sol. Cells*, Vol. 71, pp.231–243.

98 Lindgren, T., Vayssieres, L., Wang, H. and Lindquist, S.E. (2003) in Kokorin, A.I. and Bahnemann, D.W. (Eds.): *Chemical Physics of Nanostructured Semiconductors,* VSP, pp.93–126.

99 Björksten, U., Moser, J. and Grätzel, M. (1994) *Chem. Mater.*, Vol. 6, pp.858–863.

100 Morales, M.P., Gonzales-Carreno, T. and Serna, C.J. (1992) *J. Mater. Res.*, Vol. 7, No. 9, pp.2538–2545.

101 Kennedy, J.H. and Frese, K.W. (1978) *J. Electrochem. Soc*., Vol. 125, p.709.

102 Vayssieres, L. (To be published).

103 Vayssieres, L., Rabenberg, L. and Manthiram, A. (2002) *Nano Lett.*, Vol. 2, No. 12*,* pp.1393–1395.

104 McCafferty, E. (2000) *Corros. Sci.*, Vol. 42, pp.1993–2011.

105 Manjanna, J., Venkateswaran, G., Sherigana, B.S. and Nayak, P.V. (2001) *Hydrometallurgy*, Vol. 60, pp.155–165.

106 Son, M., Akao, N., Hara, N. and Sugimoto, K. (2001) *J. Electrochem. Soc.*, Vol. 148, No. 1, B43–B50.

107 Fagal, G.A., El-Shobaky, G.A. and El-Khouly, S.M. (2001) *Colloid Surf. A*, Vol. 178, pp.287–296.

108 Vayssieres, L., Guo, J.-H. and Nordgren, J. (2001) *J. Nanosci. Nanotech.*, Vol. 1, No. 4, pp.385–388.

109 Post, J.E. (1999) *Proc. Natl. Acad. Sci.*, Vol. 96, pp.3447–3454.

110 Manthiram, A. and Kim, J. (1999) *Trans. Soc. Adv. Electrochem. Sci. Technol.*, Vol. 34, pp.1–5.

111 Kannan, M. and Manthiram, A. (2002), *Electrochem. Solid State Lett.*, Vol. 5, A167–A169.

112 Kannan, M., Bhavaraju, S., Prado, F., Manivel Raja, M. and Manthiram, A. (2002) *J. Electrochem. Soc.*, Vol. 149, A483–A492.

113 Jeong, Y.U. and Manthiram, A. (2002) *J. Electrochem. Soc.*, Vol. 149, No. 11, A1419–1422.

114 Im, D. and Manthiram, A. (2003) *J. Electrochem. Soc.,* Vol. 150, pp.A68–A73.

115 Vayssieres, L., Manthiram, A. and Rabenberg, L. (To be published).

116 Minami, T. (2000) *MRS Bull.*, Vol. 25, No. 8, pp.38–44.

117 Agarwal, G. and Speyer, R.F. (1998) *J. Electrochem. Soc.*, Vol. 145, No. 8, pp.2920–2925.

118 Sousa, V.C., Segadaes, A.M., Morelli, M.R., Kiminami, R.H.G.A. (1999) *Int. J. Inorg. Chem.*, Vol. 1, pp.235–241.

119 Quaranta, F., Valentini, A., Rizzi, F.R. and Casamassima, G. (1993) *J. Appl. Phys.,* Vol. 74, No. 1, pp.244–248.

120 Schoenmakers, G.H., Vanmaekelbergh, D. and Kelly, J.J. (1996) *J. Phys. Chem. B*, Vol. 100, No. 8, 3215–3220.

121 Bagnall, D.M., Chen, Y.F., Zhu, Z., Yao, T., Koyama, S., Shen, M.Y. and Goto, T. (1997) *Appl. Phys. Lett.*, Vol. 70, No. 17, pp.2230–2232.

122 Wada, T., Kikuta, S., Kiba, M., Kiyozumi, K., Shimojo, T. and Kakehi, M. (1982) *J. Cryst. Growth*, Vol. 59, pp.363–369.

123 Klingshirn, C., Kalt, H., Renner, R. and Fodorra, F. (1985) *J. Cryst. Growth*, Vol. 72, pp.304–312.

124 Zhong, J., Kitai, A.H., Mascher, P. and Puff, W. (1993) *J. Electrochem Soc.*, Vol. 140, No. 12, pp.3644–3649.

125 Keis, K., Magnusson, E., Lindstrom, H., Lindquist, S.-E. and Hagfeldt, (2002) A. *Solar Energy Mater. Sol. Cells*, Vol. 73, No. 1, pp.51–58.

126 Keis, K., Vayssieres, L., Lindquist, S.-E. and Hagfeldt, A. (2001) *J. Electrochem. Soc.*, Vol. 148, No. 2, A149–155.

127 King, S. and Nix, R.M. (1996) *J. Catal.*, Vol. 160, pp.76–83.

128 Yoshimoto, M., Takagi, S., Umemura, Y., Hada, M. and Nakatsuji, H. (1998) *J. Catal.*, Vol. 173, pp.53–63.

129 Lehman, H.W. and Widmer, R. (1973) *J. Appl. Phys*., Vol. 44, No. 9, pp.3868–3879.

130 Rao, G.S.T. and Rao, D.T. (1999) *Sensors and Actuators*, *B*, Vol. 55, pp.166–169.

131 (a) Huang, M.H., Mao, S., Feick, H., Yan, H., Wu, Y., Kind, H., Weber, E., Russo, R. and Yang, P. (2001) *Science*, Vol. 292, pp.1897–1899; (b) Mao, S. (2004) *Int. J. Nanotechnol*., Vol. 1, Nos. 1/2, pp.42–85.

132 Vayssieres, L., Keis, K., Lindquist, S.-E. and Hagfeldt, A. (2001) *J. Phys. Chem. B*, Vol. 105, No. 17, pp.3350–3352.

133 Vayssieres, L. (2003) *Adv. Mater.* Vol. 15, No. 5, pp.464–466.

134 Vayssieres, L., Keis, K., Hagfeldt, A. and Lindquist, S.-E. (2001) *Chem. Mater.*, Vol. 13, No. 12, pp.4395–4398.

135 Vayssieres, L. (To be published).

136 Trasatti, S. (1991) *Electrochim. Acta*, Vol. 36, No. 2, pp.225–241.

137 Zheng, J.P. and Low, T.R. (1996) *J. Power Sources*, Vol. 62, pp.155–159.

138 Long, J.W., Swider, K.E., Merzbacher, C.I. and Rolison, D.R. (1999) *Langmuir*, Vol. 15, pp.780–785.

139 Jeong, Y.U. and Manthiram, A. (2001) *J. Electrochem. Soc.*, Vol. 148, No. 3, pp.A189–A193.

140 Soudan, P., Gaudet, J., Guay, D., Belanger, D. and Schultz, R. (2002) *Chem. Mater.*, Vol. 14, No. 3, pp.1210–1215.

141 Jeong, Y.U. and Manthiram, A. (2000) *Electrochem. Solid-state Lett.*, Vol. 3, No. 5, pp.205–208.

142 Vayssieres, L., Naidoo, N., Rautenbach, M., Sanderson, R. and Swart, P. (To be published).

143 Guo, J.-H. (2004) *Int. J. of Nanotechnol.*, Vol. 1, Nos. 1/2, pp.193–225.

144 Vayssieres, L., Guo, J.-H., Vayssieres, L., Persson, C., Ahuja, R., Johansson, B. and Nordgren, J. (2002) *J. Phys.: Condens. Matter.*, Vol. 14, No. 28, pp.6969–6974.

145 de Groot, F.M.F., Grioni, M., Fuggle, J.C., Ghijsen, J., Sawatzky, G.A. and Petersen, H. (1989) *Phys. Rev. B*, Vol. 40, p.5715.

146 D.W. Fisher, *J. Phys. Chem. Solids* 1971, *32*, 2455.

147 L. Qian, L. Norin, J.-H. Guo, C. Sathe, A. Agui, U. Jansson, J. Nordgren, *Phys. Rev. B* 1999, *59(19)*, 12667–12671.

148 de Groot, F.M.F., Figueiredo, M.O., Basto, M.J., Abbate, M., Petersen, H. and Fuggle, J.C. (1992) *Phys. Chem. Miner.*, Vol. 19, p.140.

149 Pedio, M., Fuggle, J.C., Somers, J., Umbach, E., Haase, J., Lindner, Th., Höfer, U., Grioni, M., de Groot, F.M.F. Hillert, B., Becker, L. and Robinson, A. (1989) *Phys. Rev. B*, Vol. 40, p.7924.

150 de Groot, F.M.F. (2001) *Chem. Rev.*, Vol. 101, No. 6, pp.1779–1808.

151 Vayssieres, L., Guo, J., Persson, C., Ahuja, R., Johansson, B. and Nordgren, J. (To be published).

152 Vayssieres, L. and Stashans, A. (To be published).